TECHNISCHE UNIVERSITÄT WIEN

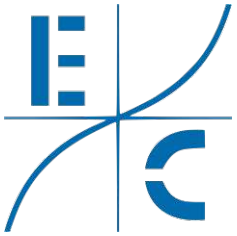

Diploma Thesis

Investigation of the Oxygen Non-stoichiometry and Phase Stability of the Lithium-ion Battery Cathode Material $LiMn_2O_4$

Institute of Chemical Technologies and Analytics

Johannes Bock, BSc

Under the supervision of

Projektass.(FWF) Dipl.-Ing. Stanislaus Breitwieser

and

Univ.Prof. Dipl.-Phys. Dr.rer.nat. Jürgen Fleig

August 2025

Contents

Abstract

Lithium manganese(III,IV) oxide ($LiMn_2O_4$) is used as a cathode material in lithium-ion batteries. There, lithium ions are reversibly inserted into the spinel-type crystal lattice, enabling the battery to charge and discharge. A disadvantage of many cathode materials is the oxygen evolution during (over-)charging, which causes safety issues due to chemical reactions with the organic electrolyte. The aim of this study is to investigate the oxygen removal and uptake of (de-)lithiated $LiMn_2O_4$ in order to relate the chemical potential of lithium with the chemical potential of oxygen, both of which affect the oxidation state of manganese.

The main method employed in this work to investigate the relation between oxygen content and chemical potential was coulometric titrations at 500 °C of both $LiMn_2O_4$ powder and sputtered thin films. For powders, self-made gas-tight cells using yttria-stabilized zirconia (YSZ) as a solid-state oxygen electrolyte were used for oxygen pumping. Thin films were deposited as working electrodes on YSZ single crystals. The voltage between this working electrode and a reference electrode was modified for oxygen titration. Additionally, the thin film samples were delithiated in an aqueous solution to assess the effect of lithiation on the oxygen removal and uptake.

Within the covered voltage range, the powder sample showed three phase transitions. XRD measurements at specific points on the titration curve showed the formation of Mn_3O_4, $LiMnO_2$ and MnO upon reduction. Re-oxidation from MnO to $LiMn_2O_4$ was found to be reversible, even though not all intermediate phase transitions were present. For the titration of the thin films, two phase transitions were observed, though shifted to higher voltages, presumably due to kinetic barriers. In addition, the delithiated samples showed instability at elevated temperatures. These measurements help to better understand the interplay between lithium and oxygen chemistry in lithium-ion battery technology.

Kurzfassung

Lithium-Mangan(III,IV)-Oxid ($LiMn_2O_4$) wird als Kathodenmaterial in Lithium-Ionen-Batterien verwendet. Lithiumionen können reversibel in Spinell-Kristallgitter eingebaut werden, um eine Batterie zu laden beziehungsweise zu entladen. Ein Nachteil von einigen Kathodenmaterialien ist die Sauerstoffentwicklung während des (Über-)Ladens, was Sicherheitsprobleme im Hinblick auf chemische Reaktionen mit organischen Elektrolyten haben kann. Das Ziel dieser Arbeit ist die Untersuchung von Sauerstoffausbau und Aufnahme von (de-)lithiiertem $LiMn_2O_4$, um das chemische Potential von Lithium mit dem chemischen Potential von Sauerstoff zu vergleichen, welche beide einen Einfluss auf die Oxidationsstufe von Mangan haben.

Die Hauptmethode, um die Beziehung von Sauerstoffgehalt und chemischem Potential zu untersuchen, war coulometrische Titration bei 500 °C von $LiMn_2O_4$-Pulver und gesputtertem Dünnfilm. Einerseits wurden selbst gefertigte gasdichte Zellen, bestehend aus Yttriumoxid-stabilisiertem Zirkonoxid (YSZ) als Festkörperelektrolyt, verwendet, um Sauerstoff zu pumpen. Andererseits wurden $LiMn_2O_4$-Dünnfilme auf YSZ-Einkristallen abgeschieden und die Spannung zwischen dieser Arbeitselektrode und einer Referenzelektrode verändert, um Sauerstoff zu titrieren. Des Weiteren wurden die Dünnfilmproben in wässriger Lösung delithiiert, um den Effekt der Lithiierung auf die Sauerstoffabgabe beziehungsweise -aufnahme zu bestimmen.

Innerhalb des untersuchten Spannungsbereichs zeigte die $LiMn_2O_4$-Pulverprobe drei Phasenübergänge. XRD-Messungen des Pulvers an konkreten Punkten der Titrationskurve zeigten die Bildung von Mn_3O_4, $LiMnO_2$ und MnO während Reduktion. Die Rückoxidation von MnO zu $LiMn_2O_4$ erwies sich als reversibel, obwohl nicht jeder einzelne Phasenübergang stattgefunden hat. Bei der Titration der Dünnfilme wurden zwei Phasenübergänge gefunden, die vermutlich aufgrund kinetischer Barrieren zu höheren Spannungen verschoben waren. Zusätzlich zeigten die delithiierten Proben Instabilität bei erhöhter Temperatur. Diese Messungen helfen dem Verständnis vom Zusammenspiel von Lithium- und Sauerstoffchemie in der Lithium-Ionen-Batterie-Technologie.

Acknowledgements

I would like to sincerely thank the entire Solid State Ionics research group of the Institute of Chemical Technologies and Analytics at the Technical University of Vienna for providing the laboratory facilities and for the great support of this diploma thesis. Thank you very much for supporting the practical experiments and sharing theoretical knowledge especially for data evaluation and interpretation. I would like to give special thanks to Projektass.(FWF) Dipl.-Ing. Stanislaus Breitwieser for his intellectual contributions as well as my main supervisor Univ.Prof. Dipl.-Phys. Dr.rer.nat. Jürgen Fleig.

1 Introduction

Lithium-ion batteries nowadays have a wide range of applications. They are not only implemented in small electronic devices such as smartphones or laptops, they are also widely used in automotives [1]. At the COP28 the United Nations Climate Change Conference in 2023 nearly 200 countries agreed to force the energy transition to reduce fossil fuels. One goal for example is to triple the renewable energy capacity by 2030. Electric vehicles play an essential role and could displace 8 million barrels of oil per day in 2030. Together with storage applications, this would lead directly to nearly 20 % of the reduction of CO_2 needed to achieve net zero emissions [2]. Today, lithium-ion batteries dominate the market of storable energy for portable electronic devices due to their numerous advantages in high specific capacity and voltage, excellent cycling stability, little self-discharge and a wide temperature range of operation [3]. The overall worldwide lithium-ion battery demand is projected to increase from 700 GW h in 2022 to 4700 GW h in 2030 [4]. Especially in the automotive sector it is forecasted that the lithium-ion battery demand for electric vehicles will increase in the next years from 1000 GW h in 2024 to 2500 GW h in 2028 [5].

Because of the importance of lithium-ion batteries in our lives, safety issues are the subject of much debate. In the UK fire accidents caused by lithium-ion batteries increased in just two years from 2022 to 2024 by 93 %, which resulted in an average of 3 fire brigade call-outs per day [6]. Undesirable side reactions caused by mechanical, thermal, or electrical abuse, cause the so-called *thermal runaway*. The root for thermal runaway can be divided into five different causes [3]:

- Heat generation leading to oxygen evolution in the cathode.
- Separator defects causing internal short circuits.
- Electrical abuse causing decomposition of the electrolyte and release of oxygen from the cathode.
- Local heat accumulation causing chemical side reactions.
- Mechanical damage causing short circuits or air entering the battery.

As listed above, overcharging as a form of electrical abuse can cause oxygen evolution of the cathode and as a further consequence fire due to chemical reaction of oxygen with the organic electrolyte [3]. To improve lithium-ion battery technology, it is therefore crucial to understand the oxygen evolution of cathode materials.

This work investigates the oxygen non-stoichiometry and phase stability of the lithium-ion battery cathode material $LiMn_2O_4$ employing solid state coulometric titrations at 500 °C. Both $LiMn_2O_4$ powder and sputtered thin films at different charge states were analysed to reveal the interplay between the chemical potential of oxygen with the chemical potential of lithium. These are linked because both chemical potentials affect the oxidation state of manganese.

2 Theoretical Background

2.1 Lithium-Ion Batteries

Lithium-ion batteries can be charged or discharged by exchange of lithium ions between an anode which usually consists of graphite (C) and a metal oxide (MO) as a cathode [7]. There are different commercial battery types widely discussed in literature [8]. They all consist of two electrodes separated by an electrolyte [7]. A schematic setup of a lithium-ion battery is shown in Figure 1.

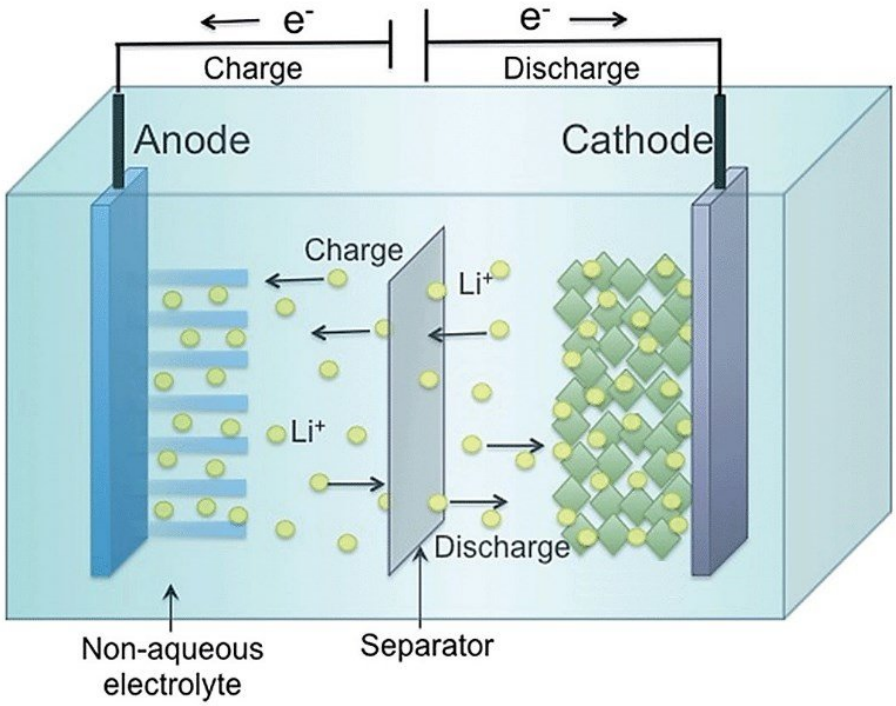

Figure 1: Schematic setup of a lithium-ion battery [9].

The general chemical reaction of discharging is shown for both electrodes in Equation 1 [7].

$$\begin{aligned} \text{Cathode:} \quad & \mathrm{Li_{1-y}MO} + y\,\mathrm{Li^+} + y\,\mathrm{e^-} \longrightarrow \mathrm{LiMO} \\ \text{Anode:} \quad & \mathrm{Li_nC} \longrightarrow n\,\mathrm{Li^+} + n\,\mathrm{e^-} + \mathrm{C} \end{aligned} \tag{1}$$

The materials used for commercial lithium-ion batteries are named in the following and are also documented in literature [9]. The most common anode material is a layered structure of graphite ($n_{\max} = \frac{1}{6}$). The cathode material varies a lot and determines the name of the battery. They differ in theoretical voltage and capacity. The most common cathode materials are Lithium Cobalt Oxide (LCO), Nickel

Cobalt Aluminium Oxide (NCA), Nickel Manganese Cobalt Oxide (NMC), Lithium Manganese Oxide (LMO) and Lithium Iron Phosphate (LFP). Layered oxide cathode materials (LCO, NCA, NMC) are primarily used and are well studied model systems [10]. Spinel-structured cathodes (e.g. LMO) however, have advantages in terms of conductivity, energy density, cost efficiency and non-toxicity [11]. The main challenge of spinel-structured cathodes is their reduced capacity at elevated temperatures [12, 13]. The electrolyte typically consists of a flammable organic solvent like ethylene carbonate, dimethyl carbonate, diethyl carbonate or ethyl methyl carbonate. To provide high ionic conductivity the electrolyte contains lithium salts like lithium hexafluorophosphate [9].

2.2 Oxygen Defect Chemistry

Defect chemistry describes the concentration and type of point defects in solids related to chemical and physical properties [14]. When a metal oxide is reduced, oxygen evolution can take place. The general formula of oxygen release of a solid crystal material written in Kröger-Vink notation is given in Equation 2 [15].

$$2\,O_O^{\times} \longrightarrow O_2(g) + 2\,V_O^{\bullet\bullet} + 4\,e' \tag{2}$$

$O_O^{\times}$ ... Oxygen atom on a regular oxygen site
$O_2(g)$ ... Molecular oxygen in gas phase
$V_O^{\bullet\bullet}$ ... Oxygen vacancy with relative charge of +2
e' ... Electron with a charge of -1

Oxygen evolution and defect chemistry is already widely understood in perovskite materials (general formula ABO_3), because these materials are used in many applications (solid oxide fuel/electrolysis cells, capacitors, piezoelectrics, sensors, etc.) and also often used as model systems. Additionally, defect chemistry in solar cell engineering is a topic of high interest, because it affects physical and chemical properties [16]. Moreover, theoretical calculations of perovskite defect chemistry are documented in literature [17]. As an example of defect chemistry in perovskite materials, in Figure 2 a so-called Brouwer diagram is shown for bulk $(La, Sr)FeO_{3-\delta}$ at 600 °C. There, defect concentrations are plotted against the oxygen partial pressure in a double logarithmic form [18]. It can be seen that for lower oxygen partial pressure the vacancy concentration increases, which means oxygen is evolving from the perovskite [18].

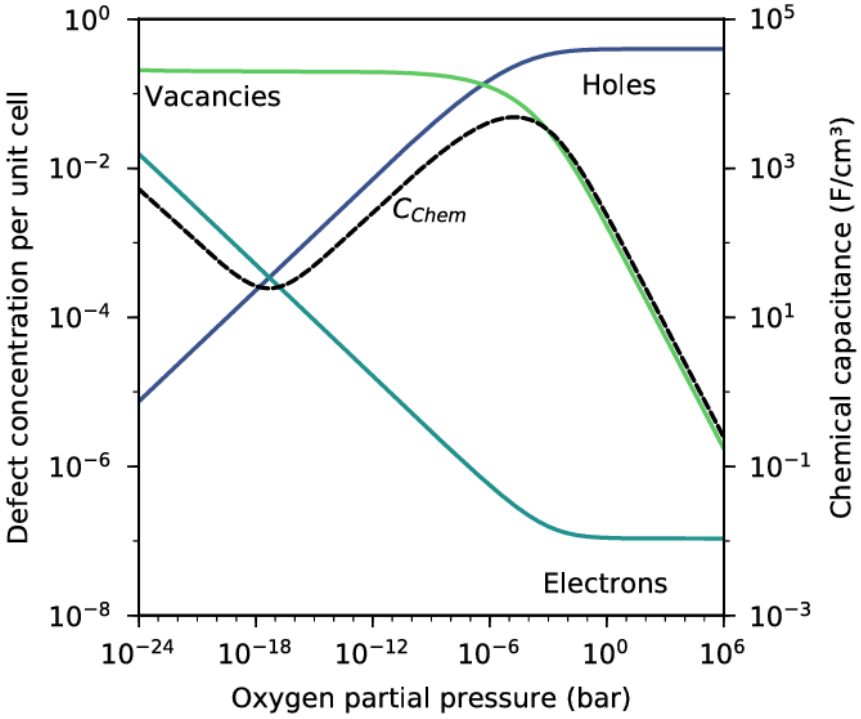

Figure 2: Brouwer diagram of bulk $(La, Sr)FeO_{3-\delta}$ at 600 °C [18].

Oxygen defect chemistry has a large influence on the oxygen reduction reaction (ORR) on perovskites as well as the oxygen evolution reaction (OER) known from water oxidation on perovskite oxides. For these reactions literature also provides proposed mechanisms [19, 20]. This knowledge is crucial, for example, for the design of solid oxide electrolysis cells to provide hydrogen as a renewable energy source [21].

2.3 Lithium Manganese(III,IV) Oxide $LiMn_2O_4$

Lithium manganese(III,IV) oxide $LiMn_2O_4$ has a spinel-type crystal lattice given in Figure 3. The structure with the space group $Fd\bar{3}m$ is well investigated in literature [22]. $LiMn_2O_4$ consists of a cubic-closed-packed oxygen lattice with octahedral and tetrahedral sites occupied by Mn- and Li-ions. Only every second octahedral site is filled with a Mn-ion and every eighth tetrahedral site is filled with a Li-ion.

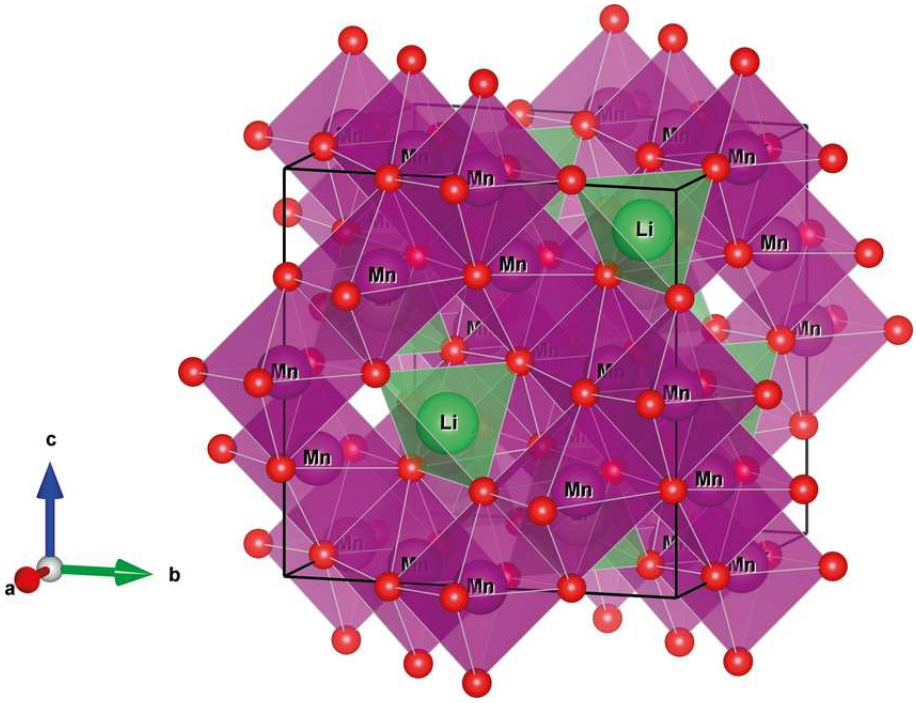

Figure 3: Spinel-type crystal lattice of $LiMn_2O_4$ [23].

In contrast to perovskite materials, defect chemistry of spinel-structured materials like $LiMn_2O_4$ is not as well investigated. However, there are theoretical computations that suggest the presence of Mn-, Li- and O-vacancies, Mn- and Li-antisites, and Li-interstitials in $LiMn_2O_4$ [24]. Their formation strongly depends on experimental conditions and the thermal history. However, it is known that pairs of defects like Li_{Mn}-Mn_{Li} are more stable than isolated defects. Also the Li-diffusion is hampered by oxygen vacancies [24].

2.4 Oxygen Evolution of Cathode Materials

In layered oxide cathode materials like LCO, high delithiation (over-charging) leads to uncoordinated oxygen which causes the formation of peroxides (O-O bonds). At temperatures around 200 °C to 250 °C O_2 is then released from the material resulting in the formation of Co_3O_4. In contrast stoichiometrical $LiCoO_2$ is much more stable up to a temperature of 900 °C [25, 26, 27]. Alloying the cathode material is a successful approach to increase structural and thermal stability. Two commercial cathode materials as an example of alloying are $LiNi_{1-x-y}Co_yAl_xO_2$ (NCA) and $LiNi_{1/3}Co_{1/3}Mn_{1/3}O_2$ (NMC) [28]. Reference [29] for example, compared the decomposition temperatures for a number of materials and found decomposition of LCO at 212 °C while NMC remained stable up to 262 °C.

Experiments concerning the phase stability of the spinel-type cathode LMO were performed by reference [30]. There, $LiMn_2O_4$ was heated up in N_2 atmosphere. Between 600 and 800 °C oxygen evolution was observed, leaving Mn_3O_4 and $LiMnO_2$ behind. Above 900 °C another oxygen release takes place, resulting in a $Li_xMn_{1-x}O$ solid solution ($x \leq 0.5$). After cooling down under 800 °C the material decomposes into two phases namely Mn_3O_4 and $LiMnO_2$. Also over-charging can lead to oxygen release in $LiMn_2O_4$, resulting in the decomposition to Mn_3O_4 [31]. The rate of these processes are strongly increased by elevated temperature [32]. While alloying with (among others) Ni can increase the stability toward oxygen evolution for LCO based materials, it decreases the stability for LMO based materials [29, 33]. $LiNi_xMn_{2-x}O_2$ (LNMO) as another commercial spinel-type cathode has higher operating voltages, but the oxygen evolution appears at lower temperatures. Especially in the delithiated state, LMO has an oxygen release onset temperature up to about 375 °C while LNMO in a charged state is already starting to release oxygen at a minimum temperature of around 300 °C [33].

Summarizing, delithiation of the cathode of lithium-ion battery forces oxygen evolution causing instabilities in the material [34, 33].

2.5 Coulometric Titration

Coulometric titration using an oxygen ion conducting electrolyte is a technique for investigating the oxygen non-stoichiometry in dependence of oxygen partial pressure and temperature. It was first used in the 1960s and is well documented in literature [35, 36]. A couple of other methods to investigate the oxygen non-stoichiometry of materials are known, such as thermo-gravimetric-analysis (TGA), volumetric measurements or neutron powder diffraction (NPD). Coulometric titration, however, has its unique selling point in its high precision and comparatively low equipment costs.

In coulometric titration, a voltage is used to drive an ionic current in an electrochemical cell. This current leads to a variation of the chemical composition in a part of the sample or setup and thus a relation between chemical potential change and charge can be obtained. There are different ways to realize this compositional change. In this thesis, two coulometric titration modes are used, one is called *gas phase coulometric titration* in the following, and the other one is named *solid state coulometric titration*.

The working principal of the gas phase coulometric titration is very much related

to an oxygen sensor in a car. It is a direct application of Nernst's Equation (Equation 3), which here describes the relation between a potential difference and a ratio of partial pressures in two different atmospheres connected via an electrolyte [37].

$$U = \frac{R \cdot T}{z \cdot F} \cdot \ln\left(\frac{p(O_2)}{p(O_2)_0}\right) \tag{3}$$

U ... Potential difference in V
R ... Ideal gas constant in $J\,mol^{-1}\,K^{-1}$
T ... Temperature in K
z ... Number of transferred electrons (in this case 4)
F ... Faraday constant in $C\,mol^{-1}$
$p(O_2)$ ... Oxygen partial pressure in bar
$p(O_2)_0$ ... Oxygen partial pressure of the reference in bar

The typical measurement setup (described in reference [35]) consists of a sample placed in a sealed titration chamber, which allows controlling of the oxygen partial pressure inside. This is achieved electrochemically by an oxygen ion conductive material, e.g. yttria-stabilized zirconia (YSZ). The reference atmosphere is in most cases air, but can also be a defined gas mixture. In contrast to an oxygen sensor in a car, the gas phase inside the coulometric titration chamber can also be modulated by pumping oxygen (see Figure 4).

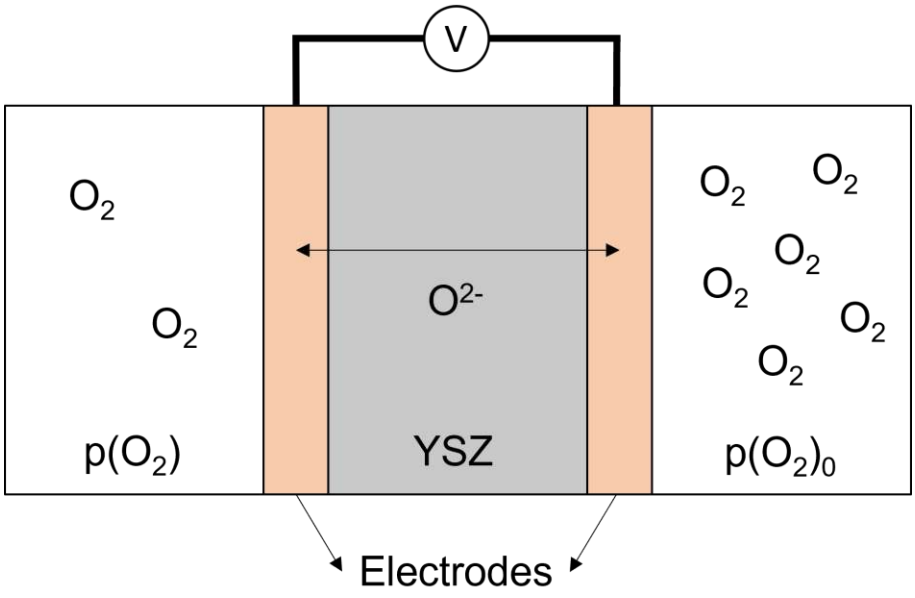

Figure 4: Sketch of an oxygen sensor cell.

Measurements can be performed via a galvanostatic or potentiostatic method [38]: In case of a galvanostatic method, a constant current is applied for a defined time and the relaxation of the voltage after the current pulse is monitored. In case of a

potentiostatic approach, the applied voltage is changed stepwise and the decaying current is measured. The resulting charge (the integration of the current over time) can then be plotted against the equilibrium voltage or calculated oxygen partial pressure. A detailed description of the data processing is given in Chapter 3.2.4.

Coulometric titration also has several error sources listed below [35]:

- Uncertainty of the potentiostat (voltage and current)
- Sample being not in an equilibrium with its atmosphere
- Electrical conduction of YSZ
- Gas phase capacity
- Gas leakage of the sealing

Corrections for the electronic conductivity of 8 mol.% Y_2O_3-ZrO_2 is possible by knowing the correlation from literature (Equation 4) [39].

$$\sigma_e = 1.31 \cdot 10^7 \cdot \exp\left(\frac{-3.88\,\mathrm{eV}}{k \cdot T}\right) \cdot p(O_2)^{-1/4} \tag{4}$$

σ_e ... electron conductivity in $\Omega^{-1}\,\mathrm{cm}^{-1}$
k ... Boltzmann constant in $\mathrm{eV\,K}^{-1}$
T ... Absolute temperature in K
$p(O_2)$ ... Oxygen partial pressure in atm

The solid state coulometric titration is essentially equivalent to the operation mode of a battery with intercalation electrodes. Instead of exposing a material to a gas phase of defined chemical potential, one electrode is used itself as the material to be investigated and its composition is changed by applying a voltage to the electrochemical cell using it as an electrode. This requires a kind of sealing. The charge or species pumped into the electrode must not leave it, in contrast to the mode used in a fuel cell. In this mode the chemical potential of the respective species, e.g. O or Li (μ_O, μ_{Li}) is given by the voltage with respect to a reference electrode via Equation 5.

$$U = \frac{\mu_x - \mu_x^{\mathrm{ref}}}{z \cdot F} \tag{5}$$

U ... Potential difference in V
μ_x ... Chemical potential of x (O or Li) in $\mathrm{J\,mol}^{-1}$
z ... Number of transferred electrons (2 for O and 1 for Li)
F ... Faraday constant in $\mathrm{C\,mol}^{-1}$

3 Materials and Methods

3.1 Powder Cells

Gas-tight titration chambers were manufactured for gas phase coulometric titration, as described in reference [40]. The titration cell consists of two parts (a lid and a base) which are both electrochemical cells on their own. A sketch of the assembled titration cell is given in Figure 5. It has three electrodes in total and allows oxygen to be pumped through the lid by applying a voltage between the counter electrode (CE) and the working electrode (WE). Oxygen partial pressure can be calculated from the voltage between the working electrode and the reference electrode (RE). Powder titration cells were fabricated from sintered yttria-stabilized zirconia (YSZ) as a solid state oxygen electrolyte with platinum (Pt) electrodes. One advantage of powder cells is that the sample - in this case $LiMn_2O_4$ (LMO) - can be measured as a powder directly and needs no further treatment.

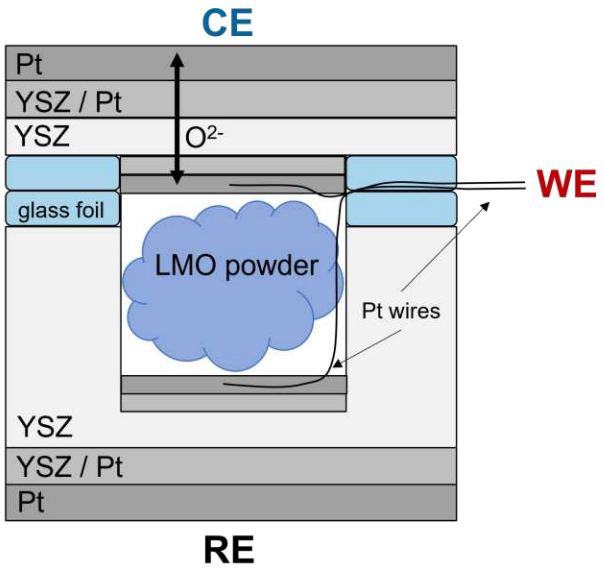

Figure 5: Sketch of a titration cell with an oxygen pumping cell between the counter electrode and the working electrode and a sensing cell between the working electrode and the reference electrode.

3.1.1 Titration Cell Preparation

YSZ powder with 8 mol.% Y_2O_3 (TOSOH®) was filled inside a silicone mould. The mould was then pressed isostatically at 15 t (3 kbar) for 1 min. The pressed pellet was then carefully sanded down to yield an even looking cylindrical shape with a typical diameter of 1 cm and a height of about 5 mm. The green body was then sintered at 1500 °C for 5 h with a heating and cooling rate of 5 °C min^{-1} and an

additional holding step during heating up at 500 °C for 2 h to remove the organic binder. The finished pellets were divided into two groups. One group was cut into thin slices of about 1 mm thickness to fabricate the top cell. In the other group a hole was milled to fabricate the bottom cell. Figure 6 depicts the produced cells.

Figure 6: Sintered YSZ pellets: Above the thin lids and below the cells with the milled cavity.

After cleaning the samples with ethanol in an ultrasonic bath, the electrodes were brushed on both sides of the lid, inside the cavity, and also at the bottom. Electrodes consisted of two layers - a mixture of YSZ and platinum and a pure platinum layer, which also acts as a current collector. The platinum layer was made out of Pt paste from TANAKA® with 7 % terpineol. For the mixed layer a 50 % mixture of this paste with the described YSZ powder in terpineol was used. In between of brushing the two layers, the samples were put in a drying oven at 120 °C to dry the paste. A platinum wire with a thickness of 0.1 mm was attached to the inside of the cavity and another one to the inner side of the lid. Then the samples were sintered at 1250 °C for 3 h with a heating and cooling ramp of 5 °C min^{-1}. The finished titration cells can be seen in Figure 7.

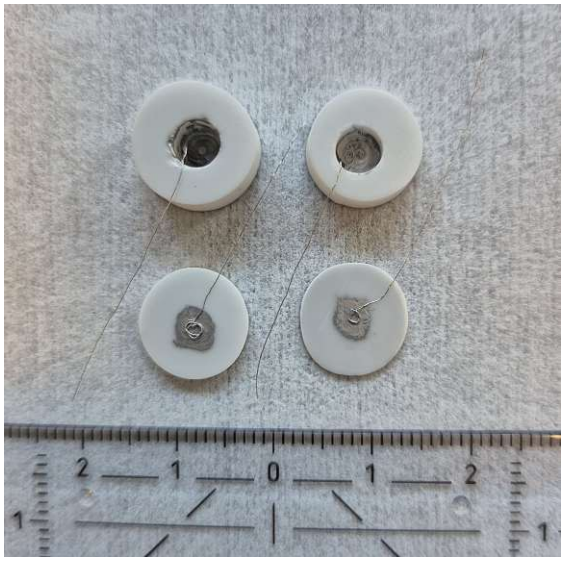

(a) Two empty cells with a scale.

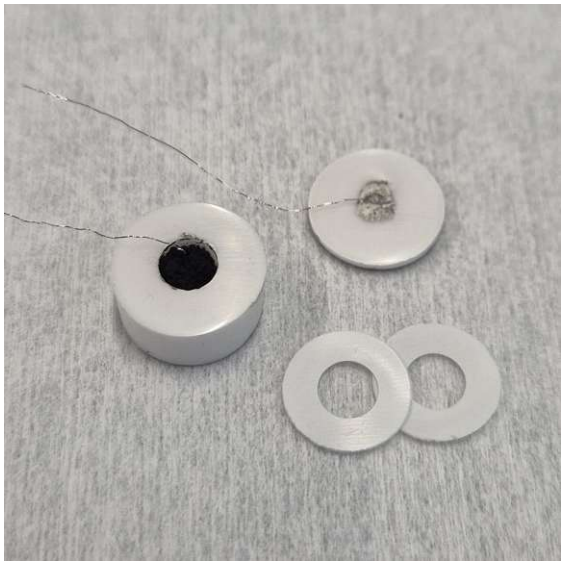

(b) One filled cell with punched glass rings.

Figure 7: Self-made dissembled titration cells.

3.1.2 Measurement of the Powder

The prepared titration cells were used to measure commercial $LiMn_2O_4$ powder for Li-ion battery cathodes (MTI KJ GROUP®). To do so the titration cell was filled with 20 - 80 mg powder. To make the cell gas-tight two rings of glass foil (KERAFOL®) were punched out and put between the cell and the lid. For sealing the cell was mounted on a self made sample stage to enable electrical contact of the electrodes (see Figure 8) and clamped to exert pressure.

Figure 8: Mounted titration cell on a self-made sample stage.

Then the mounted cell was put inside a vertical furnace and sealed with the rec-

ommended temperature programme [41] shown in Figure 9. At the end of the programme the temperature was held at 500 °C, allowing to start directly with the electrochemical measurement.

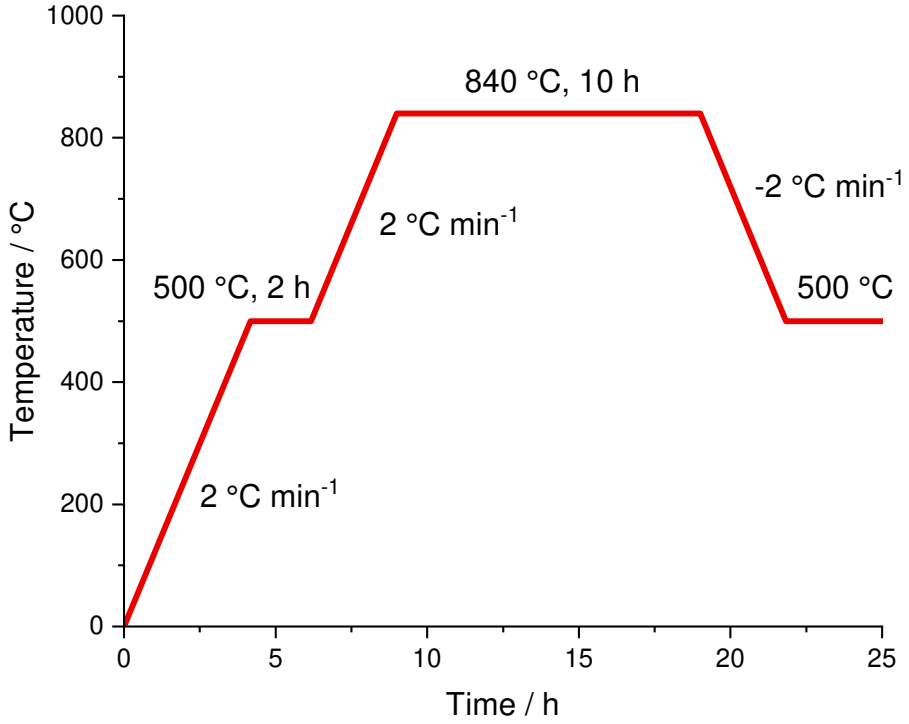

Figure 9: Temperature profile for cell sealing with glass foil.

Electrochemical measurements were performed using a SP-300 Potentiostat from BIOLOGIC®. To check the functionality of both the pumping cell and the sensing cell, electrochemical impedance spectroscopy was performed. A frequency range of 200 kHz to 10 mHz was analysed with an amplitude of 10 mV.

As the sealing of the cell takes place at a higher temperature than the following measurements, the gas phase inside the cell is initially not in equilibrium with the surrounding atmosphere. To account for that, an initializing potentiostatic step was performed by applying a constant voltage of 0 V between the working electrode and the counter electrode until an equilibrium was reached, which could be observed by measuring a current of about 0 mA.

Coulometric titration of $LiMn_2O_4$ powder was performed in an intermittent potentiostatic mode, controlling the voltage of the pumping cell. In a first step, a pre-defined charge (e.g. $Q_{\mathrm{limit}} = 0.4\,\mathrm{mA\,h}$) was pumped out of the titration chamber by applying a constant pumping cell voltage of $-1.8\,\mathrm{V}$. This was followed by an open circuit step during which the sensing cell potential (E_{WE}) was tracked. After

equilibration of the sample with the new atmosphere inside the chamber, these two steps were repeated until the designated voltage range was examined. After that, the powder was oxidized again in the same manner, but with a positive pumping voltage of +1.8 V to pump oxygen back into the cell. The whole measurement programme is listed in Table 1.

Table 1: Measurement programme of the powder sample at 500 °C.

No.	Description	Programme	Limitation
1	constant voltage	0 V vs. CE	$I \approx 0\,\mathrm{mA}$
2	constant voltage	−1.8 V vs. CE	$Q = Q_{\mathrm{limit}}$
3	open circuit	$I = 0\,\mathrm{mA}$	$E_{\mathrm{WE}} \approx$ constant
repeat steps $2-3$ until the desired E_{WE} is reached			
4	constant voltage	+1.8 V vs. CE	$Q = Q_{\mathrm{limit}}$
5	open circuit	$I = 0\,\mathrm{mA}$	$E_{\mathrm{WE}} \approx$ constant
repeat steps $4-5$ until $E_{\mathrm{WE}} = 0\,\mathrm{V}$ is reached			

In addition to the measurement of the main titration curve, the fabricated titration chambers were also used to investigate the phase composition in between phase transitions. To do so the desired voltage was applied to the pumping cell to reach a defined oxygen partial pressure inside the cell. After the measured current was approximately zero, which means E_{WE} has reached the same value than the applied voltage and an equilibrium has been reached, the sample was cooled down. To examine the phase composition of the powder, the cell was broken open with a vice (see Figure 10) and analysed via X-ray diffraction.

Figure 10: Broken cell after electrochemical measurement for analysis of the powder.

3.2 Thin Film Samples

The thin film samples for solid state coulometric titration consisted of two electrodes separated by a YSZ single crystal acting as a solid state oxygen electrolyte. A sketch of the layered structure of the thin film sample can be seen in Figure 11. At the bottom, gadolinium-doped ceria (GDC) and a mixture of GDC and platinum act as a porous counter electrode with Pt as current collector. On top, a $LiMn_2O_4$ thin film was deposited using a sputter device. Under this working electrode a gold grid was fabricated to allow full electrical contact, which was needed for delithiation. A gold layer on top acts as a current collector together with a chromium layer as an additional diffusion barrier. By contacting the electrode with a Pt wire and sealing it with glass, a voltage can be applied between the two electrodes to pump oxygen through the YSZ single crystal into or out of the LMO layer.

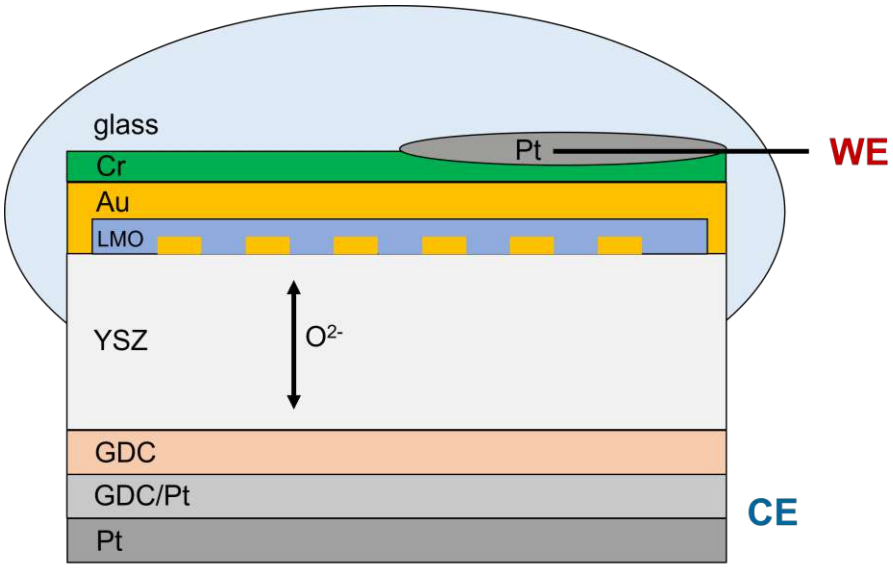

Figure 11: Sketch of the thin film sample with two electrodes allowing oxygen pumping through the YSZ single crystal.

3.2.1 Sample Preparation

The substrate of the samples are single crystals (5 x 5 x 0.5 mm) of yttria-stabilized zirconia (YSZ) with a one sided polished (100)-surface from MaTecK™. The crystals were cleaned in pure ethanol using an ultrasonic bath. For future cleaning steps between treatments some drops of ethanol were put on the samples and dried with a nitrogen flow.

To fabricate the counter electrode, a paste of 10 % gadolinium-doped ceria (GDC) form TREIBACHER® with the chemical composition $Gd_{0.1}Ce_{0.9}O_{1.95}$ in terpineol

was used. The paste was applied to the unpolished side of the single crystal via spin coating (678 Hz for 1 min). After drying at 120 °C, a 50 % mixture of GDC paste and platinum paste (described in Chapter 3.1.1) was brushed on top. After another drying step, platinum paste as a current collector layer was brushed on top. The samples were sintered at 1150 °C for 3 h with a heating ramp of 5 °C min^{-1}.

On the polished side of the single crystal a thin gold layer of about 150 - 200 nm was sputtered in an 2×10^{-2} mbar argon atmosphere with a current of 100 mA using the BAL-TEC MED 020 Coating System (see Figure 12). To ensure thermal stability of the gold grid, the process was performed at elevated temperatures.

Figure 12: BAL-TEC MED 020 Coating System.

The gold grid was fabricated using photolithography. One drop of photoresist was put on the gold layer and spin coated with 100 Hz for 40 s followed by 60 Hz for 15 s. Then the sample was put on a heating plate at 100 °C for 4 min. A glass mask with a 5 × 15 square grid was put on the sample and exposed to UV-light with a power of 350 W for exactly 30 s. The sample was etched in a developer solution for 30 - 50 s and then the etching process was stopped by putting the sample in H_2O. Under a microscope the resist grid was checked if the etching process was completed. The sample was then ready for ion beam etching. In this process the sample was sputtered with argon atoms, removing the gold layer where no resist was on top. Finally, the resist was removed using ethanol leaving a gold grid on the polished side of the single crystal shown in Figure 13.

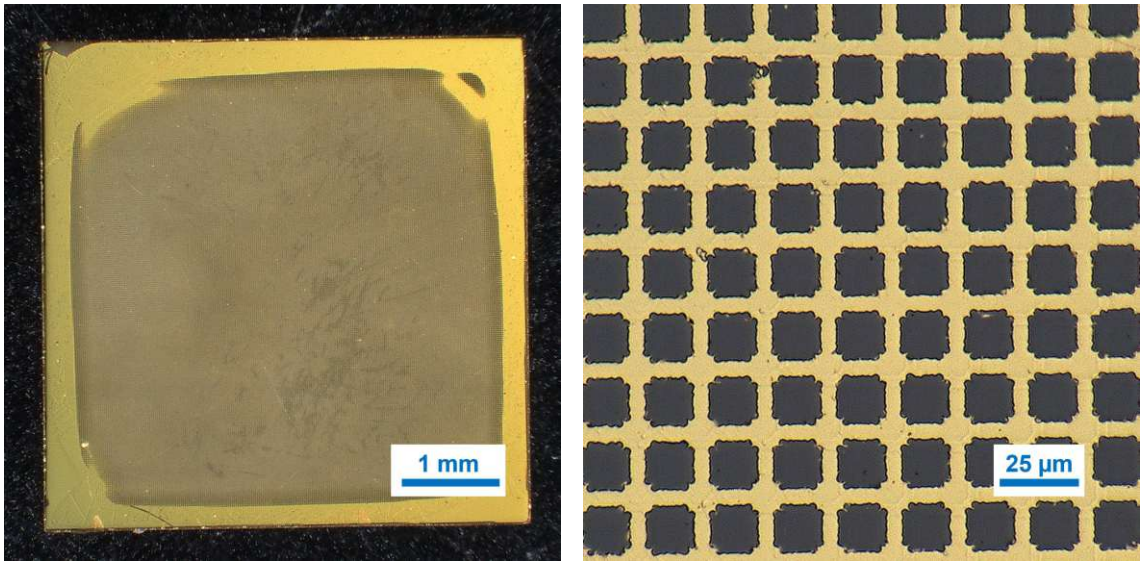

(a) Magnification of 30x.

(b) Magnification of 1000x.

Figure 13: Light microscope image of the gold grid.

The next step was to deposit a layer of $LiMn_2O_4$ from a target of the same composition with an in-house built magnetron RF-sputter device, which is shown in Figure 14. The deposition took place at 640 °C with a pressure of 2.5×10^{-2} mbar (75 % Ar and 25 % O_2) for 3 h with a power of 60 W as described in reference [42]. A 4×4 mm mask was used to cover the edges. The exact area of the deposited layer was measured in a light microscope afterwards. The thin film had a thickness of 200 - 300 nm with a large roughness determined with a profilometer.

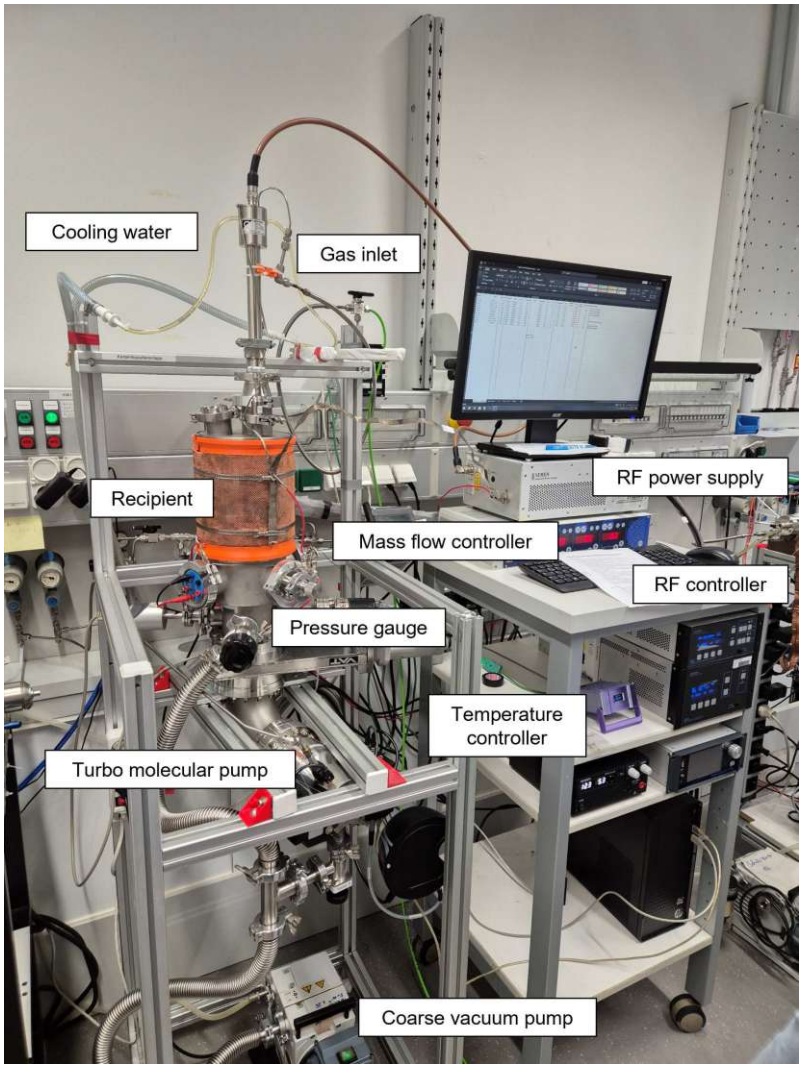

Figure 14: Ceramic magnetron RF-sputter device.

Some samples were delithiated in an aqueous solution of $1\,\mathrm{mol\,L^{-1}}$ $LiNO_3$ using a three electrode setup shown in Figure 15. A voltage ramp of $1\,\mathrm{mV\,s^{-1}}$ between the sample and the platinum counter electrode was applied to reach and hold a defined constant positive voltage between the sample and the Ag/AgCl reference electrode until an equilibrium was reached. Two different voltages were tested: $+0.8\,\mathrm{V}$ and $+1.0\,\mathrm{V}$ vs. Ag/AgCl. The equilibrium was determined by the measured current approaching a value of approximately zero.

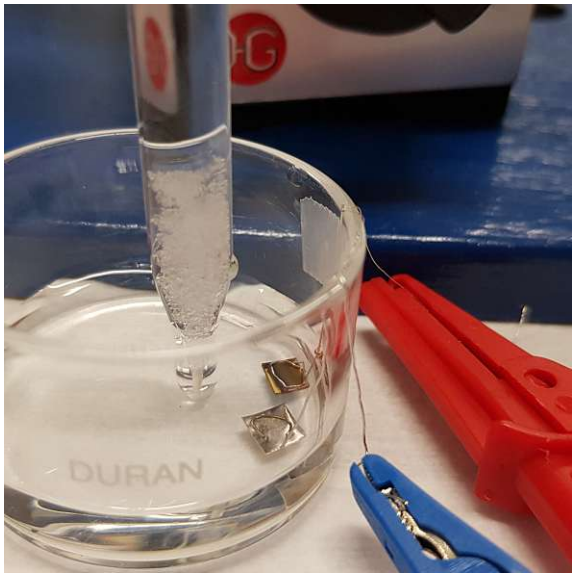

Figure 15: Delithiation of the sample using a Pt counter electrode and a Ag/AgCl-reference electrode.

On top of the $LiMn_2O_4$ layer a 500 nm gold layer was deposited with the BAL-TEC MED 020 Coating System in a similar manner as described above. This was followed by a 250 nm chromium layer, deposited with 7×10^{-3} mbar argon and a current of 100 mA. Before proceeding further, the edges of the single crystal were sanded down with sandpaper to remove any metallic depositions on the edges causing potential short circuits between the two electrodes. A 0.1 mm thick platinum wire was attached on top of the chromium layer with platinum paste and sintered at 800 °C for 6 h. The samples were then ready for sealing with a paste made out of alkalifree barium-borate-glass powder from SCHOTT® suspended in terpineol. The paste was brushed on top and also on the edges of the sample and then sintered with the recommended temperature programme [43] at 700 °C for 30 min with a heating and cooling ramp of $1\,°C\,min^{-1}$ to avoid glass cracks. The finished sample was mounted on a measurement stage shown in Figure 16.

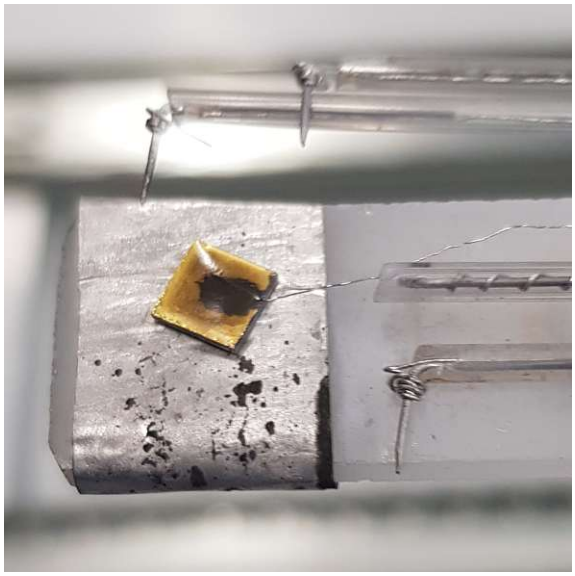

Figure 16: Thin film sample mounted on the measurement stage.

3.2.2 Characterisation

For characterisation of the morphology, determination of the sputter rate and analysis of the lithium amount before and after the delithiation in the thin films, reference samples were produced. These samples were produced in a similar manner as the thin film samples, but without a counter electrode, a gold/chromium top layer and a glass sealing. This time larger YSZ single crystals ($10 \times 10 \times 0.5\,\mathrm{mm}$) with a one sided polished (100)-surface from CrysTec™ were used to have more sample material for quantification. The thin film was characterised with a profilometer from BRUKER®, a scanning electron microscope and X-ray diffraction.

Moreover, the lithium amount was quantified with inductive coupled plasma mass spectrometry (ICP-MS). For that, the sample was treated with 1 mL of a 50 : 50 mixture of HCl and HNO_3 in a test tube and heated in a 90 °C hot water bath to dissolve the sputtered thin film. The solution was diluted with H_2O to reach a total volume of 10 mL. 5 µL of a 1000 ppm indium solution was added as an internal standard. Every sample was then diluted with 1.5 % HNO_3 to yield a 1:100 and a 1:1000 dilution. Together with reference samples for calibration the solutions were measured with a triple quadrupole iCAP™ TQ ICP-MS from THERMO SCIENTIFIC™ to calculate the elemental composition.

3.2.3 Measurement of the Thin Film

For the solid state coulometric titration, the sample was mounted on a sample stage connected to a SP-300 Potentiostat from BIOLOGIC®. The platinum counter electrode was contacted with a platinum sheet and the platinum wire contacting the working electrode was attached to a platinum needle (Figure 16). Then the sample was inserted into a furnace. Before starting the measurement, the sample was in situ sealed to remove potential glass cracks. For that, the oven was heated to 700 °C with a ramp of 1 °C min^{-1}. After 30 min the furnace was cooled down to 500 °C with the same heating ramp of 1 °C min^{-1}. The measurement programme consisted of potentiostatic steps and can be seen in Table 2. The voltage between the working electrode and the counter electrode was changed in 50 mV steps. After each step the voltage was held constant to reach an equilibrium. Before jumping to the next voltage change an impedance spectrum (10 kHz to 10 mHz with an amplitude of 10 mV) was measured. After a voltage of −1.2 V vs. air had been reached, the programme continued in the opposite direction to reach again a voltage of 0 V vs. air. The whole programme took about 150 h.

Table 2: Measurement programme of the thin film samples at 500 °C. E_{control} stands for the previously applied voltage.

no.	Description	Programme	Time
1	constant voltage	0 V vs. CE	1 h
2	voltage scan	−10 mV s^{-1} vs. CE	5 s
3	constant voltage	0 V vs. E_{control}	3 h
4	impedance spectrum	10 kHz to 10 mHz	11.3 min
repeat steps 2 − 4 until −1.2 V vs. CE is reached (24 times in total)			
5	voltage scan	10 mV s^{-1} vs. CE	5 s
6	constant voltage	0 V vs. E_{control}	3 h
7	impedance spectrum	10 kHz to 10 mHz	11.3 min
repeat steps 5 − 7 until 0 V vs. CE is reached (24 times in total)			

3.2.4 Data Processing

The described programme is also illustrated in Figure 17. As an example the first three steps are shown. A negative potential jump results in a negative current spike. Normally the current reaches a constant level corresponding to leakage of oxygen through the glass sealing. This leak current is voltage dependant and needs to be determined to correct the measured charge for contributions of gas leakage.

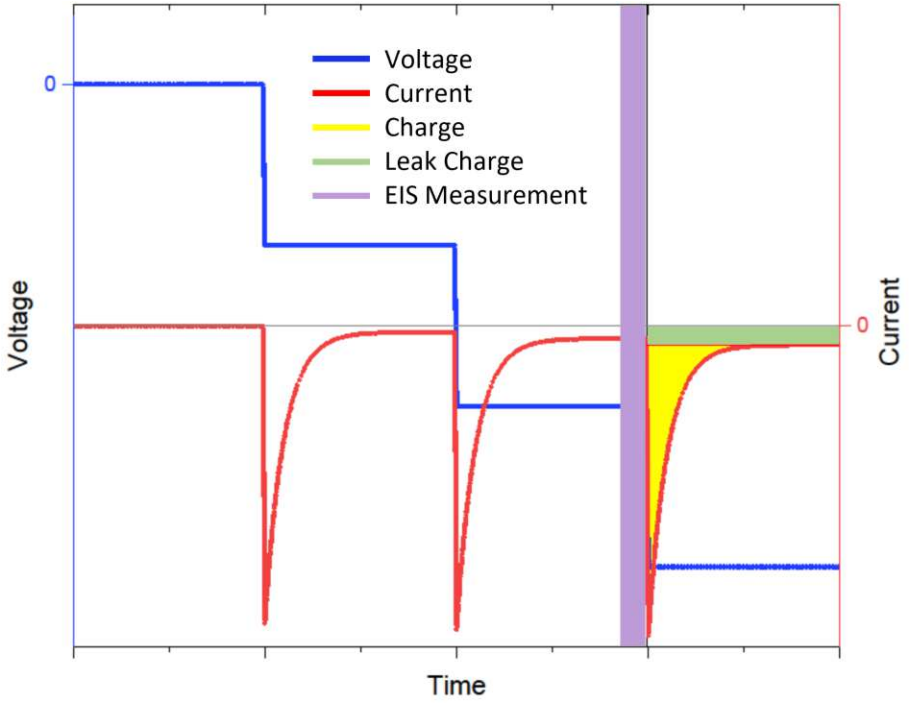

Figure 17: Schematic diagram of the thin film measurement programme.

The data evaluation and processing was done with a self-written Python script and will be explained in the following on the basis of one sample. In Figure 18 the raw data of voltage and current is plotted over measurement time. There the applied voltage steps can be seen, together with their corresponding current spike. A negative voltage step during reduction resulted in a negative current spike. A positive voltage step during (re-)oxidation resulted in a positive current spike. In each step the current should reach a constant value, which corresponds to leakage of the glass sealing. While the measured current was in the µA range, the leak current was in the nA range, allowing for a good separation of both contributions.

One might ask, why it looks like the current spikes (in the raw data in Figure 18) are in both directions despite only one voltage step. This is caused by the impedance spectrum that was measured after each voltage step. During switching from EIS to the voltage ramp, only the first data points were recorded with a potential wrong

sign of the current. In the zoomed images of Figure 18 the detailed behaviour of the current in one single step can be seen.

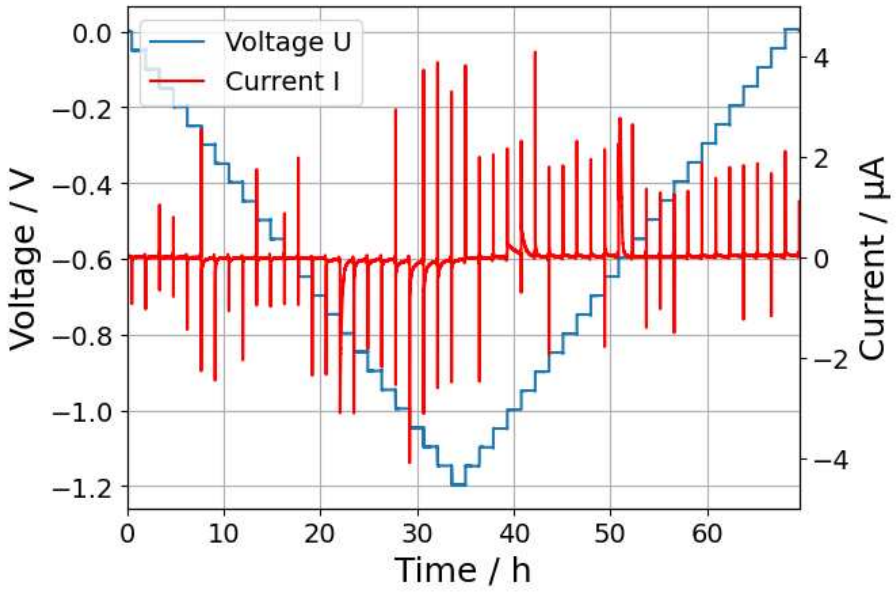

(a) Overview of one whole cycle.

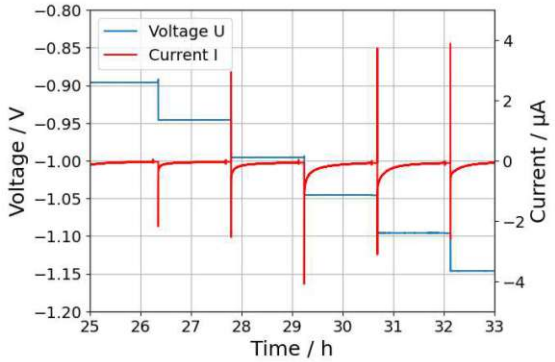

(b) Zoomed image during reduction.

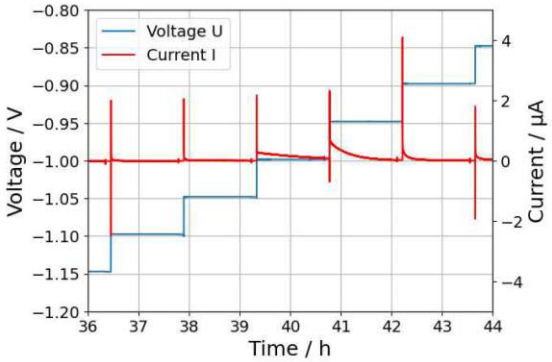

(c) Zoomed image during oxidation.

Figure 18: Raw data of one solid state coulometric titration program.

For every voltage step a corresponding leak current was calculated by averaging the last 1 % of the measured current data points. The charge for each step was calculated by integrating the current minus the leak current over time using Equation 6. In addition, the charge was normalized to the sample volume for better comparison between different samples.

$$Q = \int I - I_{\text{leak}}\, dt \tag{6}$$

Q ... Charge per step in mA s
I ... Measured current in mA
I_{leak} ... Leak current in mA

For slow processes (for instance phase transitions) the chosen step time may not be long enough to allow for a full equilibration of the sample. In these cases, the described method to determine the leak current will result in an overestimation. To account for this, leak currents that strongly differed from leak currents at similar voltages were excluded from the evaluation. Leak current values for these voltage steps were then obtained by linear interpolation of neighbouring leak currents. This process is illustrated in Figure 19, where overestimated leak currents are visible as peaks.

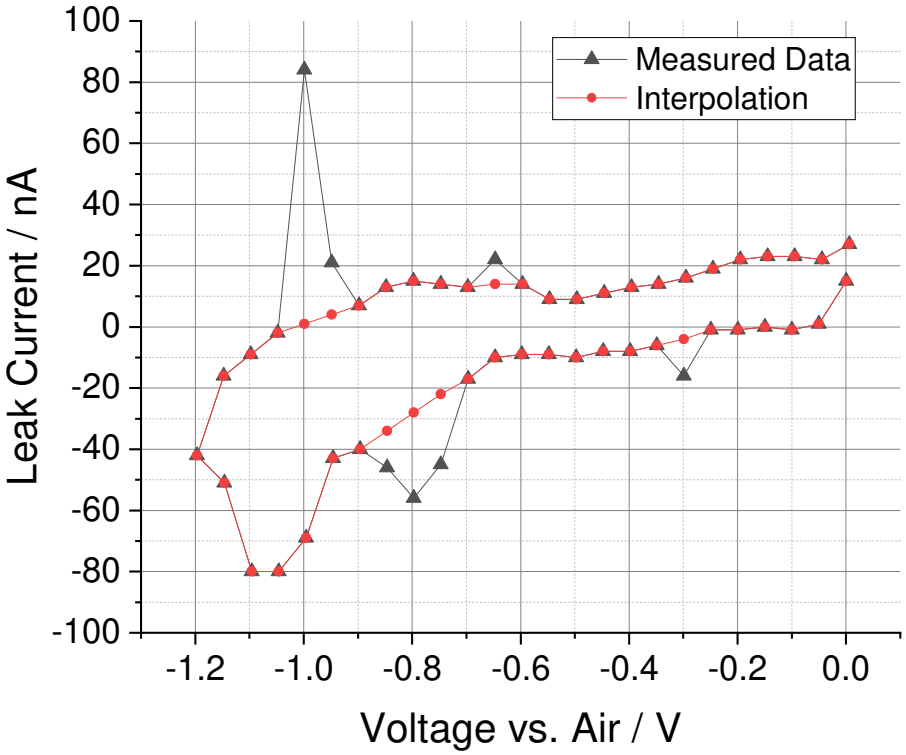

Figure 19: Leak current and its linear interpolation.

The effect of the leak current correction and the difference between using the interpolation of the leak current can be seen in Figure 20. For the following presentation and discussion of the results, a leak current correction with interpolation was performed.

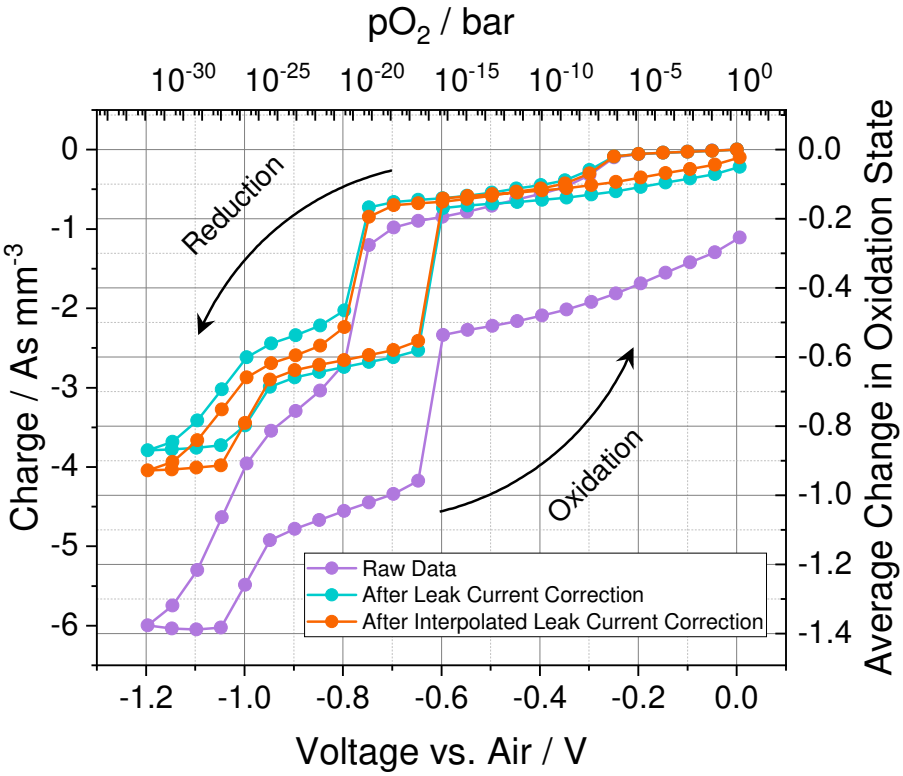

Figure 20: Comparison of the leak current correction (with and without the interpolation of the leak current) with the raw titration curve.

4 Results and Discussion

4.1 $LiMn_2O_4$ Powder

4.1.1 Titration Cell Characterisation with EIS

To ensure the functionality of the titration chamber setup, electrochemical impedance spectroscopy of both the pumping cell and the sensing cell was performed. Each cell consisted of a YSZ electrolyte and two electrodes as described in Chapter 3.1. The electrolyte was modelled with a resistance. The electrodes were modelled with two RC-elements. A constant phase element (CPE) was chosen instead of a regular capacitor to account for non idealities of the electrodes. The results (including the used equivalent circuit for fitting) are given in form of a Nyquist plot and a Bode plot in Figure 21.

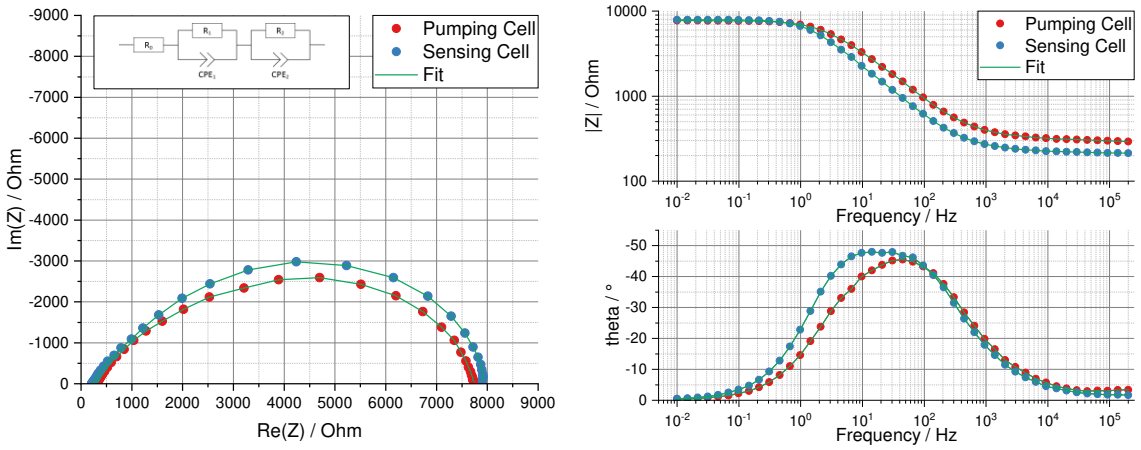

(a) Nyquist plot.

(b) Bode Plot.

Figure 21: Electrochemical impedance spectroscopy of the empty titration cell at 500 °C.

The results of the mathematical fitting are listed in Table 3. Generally it can be seen that the values for the pumping cell and the sensing cell are very similar. This was expected since both cells consisted of YSZ/Pt-electrodes fabricated in the same way.

Table 3: Fitting values of electrochemical impedance spectroscopy of an empty titration cell.

	Pumping Cell		Sensing Cell	
Element	Value	Error / %	Value	Error / %
R_0 / Ω	300	0.4	216	0.3
R_1 / Ω	4552	41	2451	16
R_2 / Ω	2944	62	5309	7
CPE_1-T	1.6E-05	20	3.0E-05	5
CPE_1-P	0.69	1.8	0.69	0.5
CPE_2-T	2.3E-05	41	2.0E-05	6
CPE_2-P	0.95	11.3	0.94	1.8

4.1.2 Gas Phase Coulometric Titration

To study the oxygen defect chemistry in $LiMn_2O_4$, a gas phase coulometric titration was performed at 500 °C. The main titration curve of 70.5 mg $LiMn_2O_4$ powder can be seen in Figure 23. There, the charge for each step is plotted against the equilibrium voltage which corresponds to a oxygen partial pressure via Equation 7.

$$p(O_2) = p(O_2)_0 \cdot e^{\frac{4 \cdot F}{R \cdot T} \cdot U} \tag{7}$$

$p(O_2)$ ... Oxygen partial pressure inside the cell in bar
$p(O_2)_0$ ... Oxygen partial pressure outside the cell in bar
F ... Faraday constant in $C\,mol^{-1}$
R ... Ideal gas constant in $J\,mol^{-1}\,K^{-1}$
T ... Temperature in K
U ... Voltage between the electrodes of the sensing cell in V

As the amount of $LiMn_2O_4$ inside the titration chamber is known, the charge axis can be transformed into an average oxidation number of manganese, based on the assumption that initially an average oxidation state of 3.5 is present. The formula used for this conversion is shown in Equation 8.

$$ON_{av} = 3.5 + \frac{Q \cdot M}{2 \cdot F \cdot m} \tag{8}$$

ON_{av} ... Average oxidation number of manganese
Q ... Charge in C (here negative)
M ... Molar mass of $LiMn_2O_4$ in $g\,mol^{-1}$
F ... Faraday constant in $C\,mol^{-1}$
m ... Mass of $LiMn_2O_4$ in g

The charge corresponding to the compositional change of the gas phase towards lower pressures is negligible here. Assuming a maximum gas volume of 0.1 mL, the amount of oxygen at 1 bar and 500 °C corresponds to a charge of 0.17 mA h, which

was calculated according to Equation 9.

$$Q = \frac{4 \cdot F \cdot p \cdot V}{R \cdot T} \tag{9}$$

Q ... Charge in C
F ... Faraday constant in $\mathrm{C\,mol^{-1}}$
p ... Pressure in Pa
V ... Volume in $\mathrm{m^3}$
R ... Ideal gas constant in $\mathrm{J\,mol^{-1}\,K^{-1}}$
T ... Temperature in K

Please note that slow equilibration of the powder with the gas phase required very long measurement times. Equilibration depends very much on the oxygen partial pressure. For example, at a potential of around $-0.2\,\mathrm{V}$ the equilibration for one step took hours (see Figure 22a) in contrast to a potential of around $-0.9\,\mathrm{V}$, where one equilibration step took days (see Figure 22b).

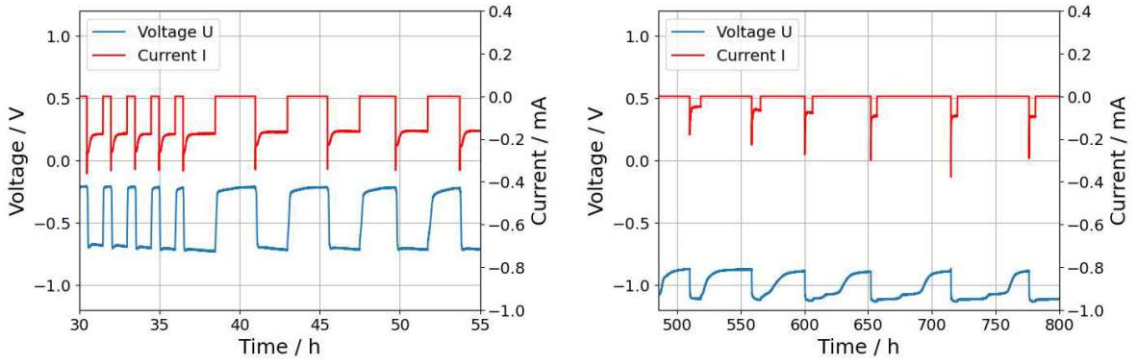

(a) Zoomed image of the raw data at a potential of around $-0.2\,\mathrm{V}$.

(b) Zoomed image of the raw data at a potential of around $-0.9\,\mathrm{V}$.

Figure 22: Raw data of the gas phase coulometric titration.

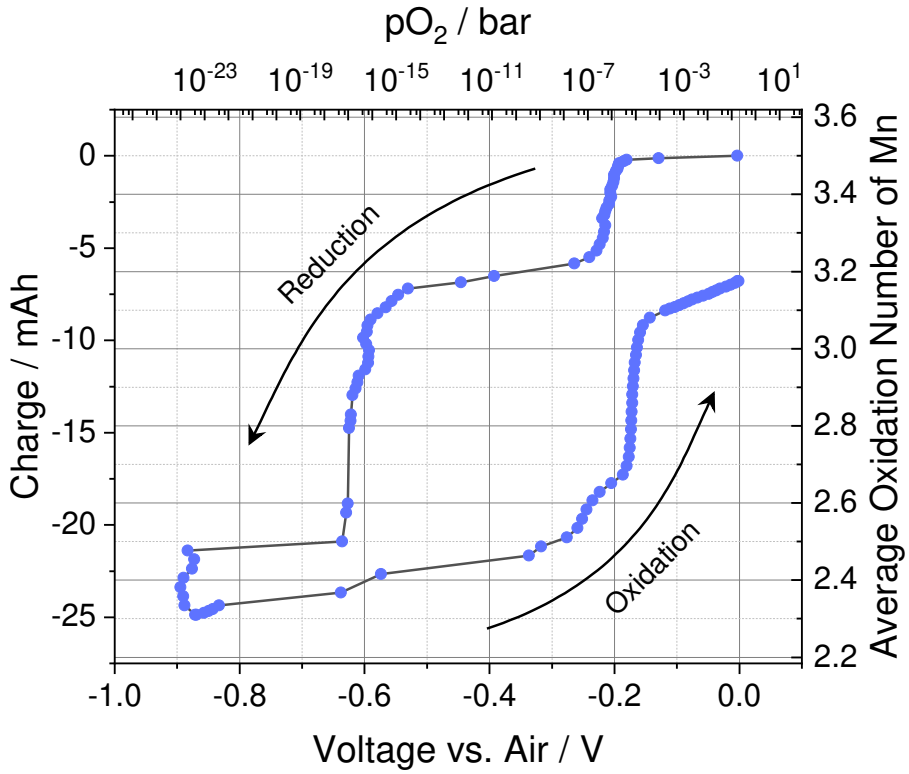

Figure 23: Coulometric titration curve of $LiMn_2O_4$ powder.

For the reduction of $LiMn_2O_4$ there are three points in this curve where a change in charge at an almost constant voltage was observed. The first one is located at a potential of about $-0.2\,V$ (10^{-6} - 10^{-7} bar), the second at a potential of $-0.6\,V$ (10^{-17} bar), and the last one is located at a potential of $-0.9\,V$ (10^{-24} bar). Upon re-oxidation only at one point a change in charge is observable at an almost constant voltage. The charge for the whole reduction and oxidation cycle is not fully reversible.

This means there are three points within the covered voltage range where oxygen is removed from the crystal lattice without changing the equilibrium atmosphere inside the titration chamber. The points where the charge changes without a large change of the potential are considered to be phase transitions of the sample [44]. The last phase transition was probably not finished within the measurement range. During re-oxidation in the opposite direction, only one huge phase transition could be observed. The charge gap at the end of the measurement might be due to little gas leakage over the whole titration. The large hysteresis present in this curve might be caused by the different kinetics of the specific reduction and oxidation reactions. In between of phase transitions, for example at an average oxidation number of Mn of +3.2 on reduction direction, a kind of plateau can be seen with a gradual change

of the charge. This could be an indication of oxygen non-stoichiometry in the crystal lattice of the sample. The slope in the beginning of the reduction of $LiMn_2O_4$ is very low. This means that for pure $LiMn_2O_4$ only very small oxygen non-stoichiometry would be observable. In the range of $-0.25\,V$ to $-0.55\,V$ the slope is larger, which indicates oxygen non-stoichiometry more clearly. A change of the average oxidation number of Mn corresponds to the same δ in the oxygen content of $LiMn_2O_{4-\delta}$. An overall change in average oxidation number of about 0.05 for example corresponds to 1.25 % oxygen vacancies, neglecting the presence of other phases.

4.1.3 XRD Analysis at Different Titration States

To investigate the measured phase transitions and reveal the phase composition of the powder, X-ray diffraction of the powder was measured at different states on the titration curve. The samples were quenched at the following potentials vs. air and the resulting diffractogramms are shown in Figure 24-27:

- 0 V (native powder before titration)
- $-0.40\,V$ (10^{-11} bar)
- $-0.75\,V$ (10^{-20} bar)
- $-1.25\,V$ (10^{-35} bar)
- 0 V (powder after a whole titration cycle)

At $-0.40\,V$ (10^{-11} bar) the powder diffractogram (Figure 24) shows two phases ($LiMn_2O_4$ and Mn_3O_4). Rietveld refinement calculated the mass percentage of each phase to 74 % $LiMn_2O_4$ and 26 % Mn_3O_4. This results in 78 mol % $LiMn_2O_4$ and 22 mol % Mn_3O_4 (ratio of around 3.5 : 1).

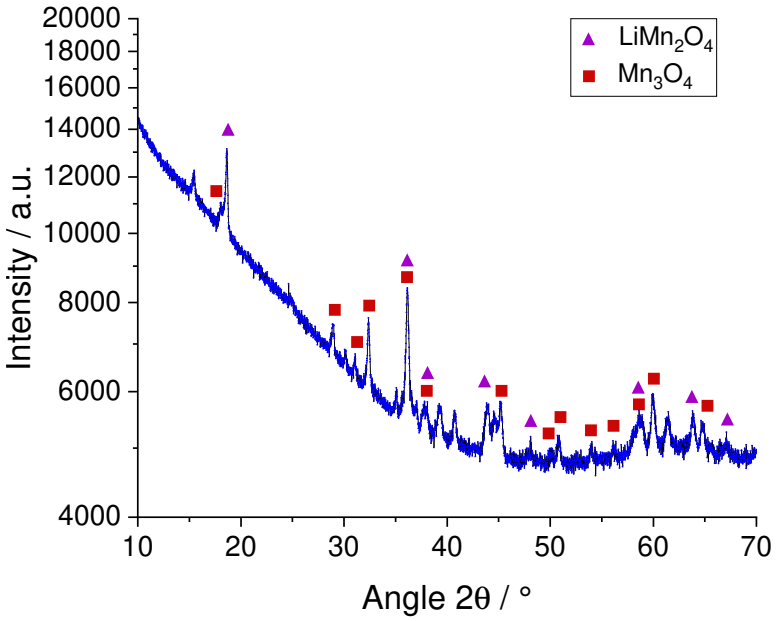

Figure 24: X-ray diffractogram of the powder at an oxygen partial pressure of 10^{-11} bar.

The Li-Mn-O phase diagram includes a large number of different phases and many different phase transitions have been reported [45, 46]. However, most probably Li is enriched in the spinel phase and thus $Li_{1+x}Mn_{2-y}O_{4-z}$ might result. A possible phase transition is given in Equation 10.

$$10\,LiMn_2O_4 \longrightarrow 7\,Li_{10/7}Mn_2O_4 + 2\,Mn_3O_4 + 2\,O_2 \tag{10}$$

This equation results in an average oxidation number of Mn of +3.1 and a ratio between spinel phase and Mn_3O_4 of 3.5 : 1, which is in excellent accordance with the Rietveld refinement. In addition, the average oxidation number of Mn fits pretty well the value of the corresponding plateau (around +3.2). Even though Mn deficiencies in the spinel are reported in literature, this does not fit very well to our reported change in charge. In Equation 11, for example, the average Mn oxidation number does not change at all.

$$4\,LiMn_2O_4 \longrightarrow 3\,Li_{4/3}Mn_{5/3}O_4 + Mn_3O_4 \tag{11}$$

At −0.75 V (10^{-20} bar) the powder diffractogram (Figure 25) shows two new phases ($LiMnO_2$ and MnO). Rietveld refinement calculated a composition (in mass percentage) of 48 % $LiMnO_2$ and 52 % MnO. This results in 41 mol % $LiMnO_2$ and 59 mol % MnO (ratio of about 1 : 1.4).

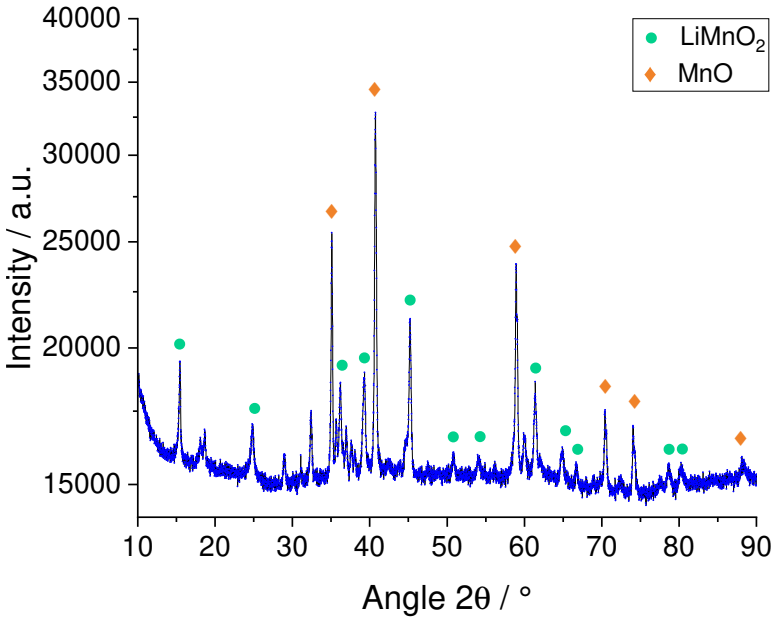

Figure 25: X-ray diffractogram of the powder at an oxygen partial pressure of 10^{-20} bar.

For this phase transition a possible chemical reaction is given in Equation 12.

$$7\,Li_{10/7}Mn_2O_4 + 2\,Mn_3O_4 \longrightarrow 10\,LiMnO_2 + 10\,MnO + 3\,O_2 \tag{12}$$

This would lead to a ratio between $LiMnO_2$ and MnO of $1:1$ and an average oxidation number of Mn of +2.5 which perfectly fits the change in charge in the titration curve. There, the second plateau is also located at an average oxidation number of Mn of +2.5. Interestingly, the transition voltage of around $-0.65\,V$ is also close to the voltage vs. 1 bar O_2 at which Mn_3O_4 and MnO coexist ($-710\,mV$) [47]. Actually, the reaction in Equation 12 consists of two phase transitions, Mn_3O_4/MnO and $Li_{10/7}Mn_2O_4$/$LiMnO_2$,MnO, which seem to take place at very similar voltages and are not separable.

Although the titration curve was only measured until a potential of $-0.9\,V$, an additional sample was reduced to a potential of $-1.25\,V$ (10^{-35} bar). The diffractogram of this sample is shown in Figure 26.

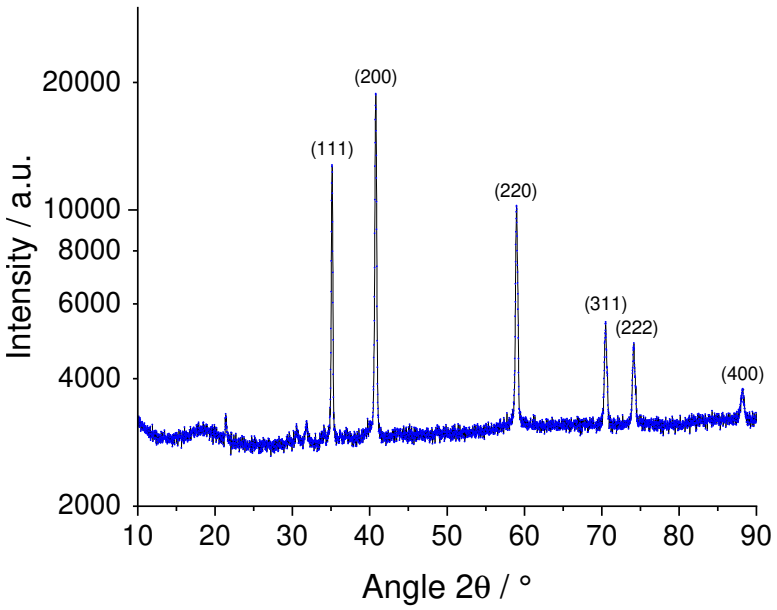

Figure 26: X-ray diffractogram of the powder (MnO) at an oxygen partial pressure of 10^{-35} bar.

At this point only MnO was observed without additional impurities. The colour of the MnO powder was brown/black in comparison to the native $LiMn_2O_4$ powder, which was dark blue/black. Unavoidably, also a Li-containing oxide must be present, probably Li_2O (or Li_2CO_3). This, however, was not detected in XRD. The supposed reaction is given in Equation 13.

$$4\,LiMnO_2 \longrightarrow 4\,MnO + 2\,Li_2O + O_2 \tag{13}$$

These results clearly suggest that the last phase transition visible in the titration curve is the formation of MnO, though the reaction is possibly not yet completed when switching to the re-oxidation (the average oxidation number of Mn of +2.3 is still larger than expected for MnO).

Finally, Figure 27 shows the comparison between the powder before coulometric titration and after a whole titration cycle. There, hardly any differences are observable.

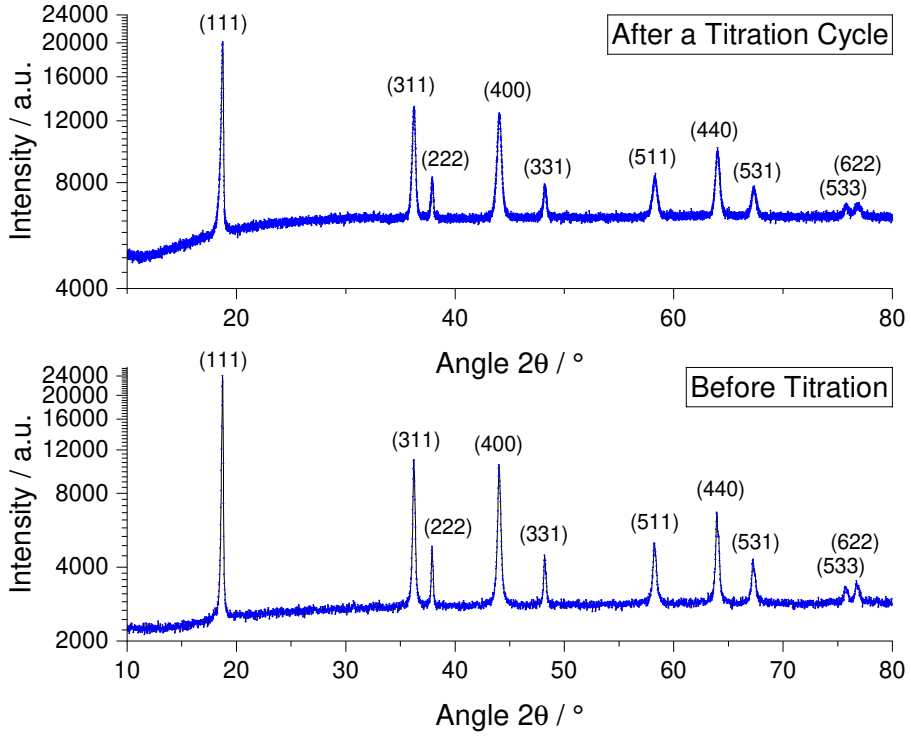

Figure 27: Comparison between native $LiMn_2O_4$ powder with the powder after a titration cycle.

The calculated compositions together with the suggested chemical reactions for the phase transitions match the measured average oxidation number of manganese very well within the precision of Rietveld refinement. A highly interesting observation is that the re-oxidation to $LiMn_2O_4$ is completely reversible. This means the previously discussed charge gap is most probably caused by gas leakage. The observed phase transitions summarized in Figure 28 are similar to the phase transitions in case of thermal reduction described in Chapter 2.4 known from literature [30].

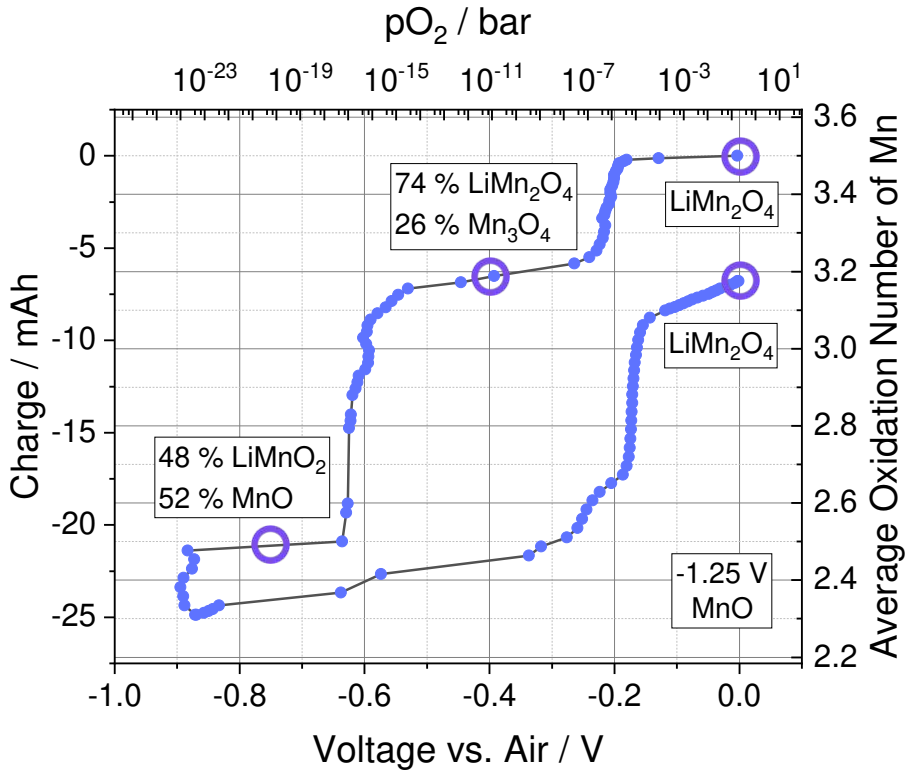

Figure 28: Summary of the XRD measured phases on the titration curve. The numbers indicate mass percentages deduced by Rietveld refinement for the given compositions.

In summary, at a potential of $-0.2\,\mathrm{V}$ $LiMn_2O_4$ partially decomposes to Mn_3O_4. At a potential of around $-0.6\,\mathrm{V}$ the powder decomposes into two new phases ($LiMnO_2$ and MnO), which means that more than one phase transition takes place simultaneously. Different reaction paths are taken for reduction and oxidation. The oxidation back to $LiMn_2O_4$ largely takes place at only one potential of about $-0.2\,\mathrm{V}$, which is the same where the first reduction of $LiMn_2O_4$ takes place. Probably, $LiMnO_2$ is not formed (from Li_2O and MnO) during oxidation. The shoulder-like feature at around $-0.25\,\mathrm{V}$ might indicate at least some initial formation of the Li-rich spinel.

4.2 $LiMn_2O_4$ Thin Film

4.2.1 Characterisation of the Morphology

A profilometer was used to determine the average thickness of the sputtered thin film on a reference sample with a free edge. The sample itself and the result of the measurement are shown in Figure 29.

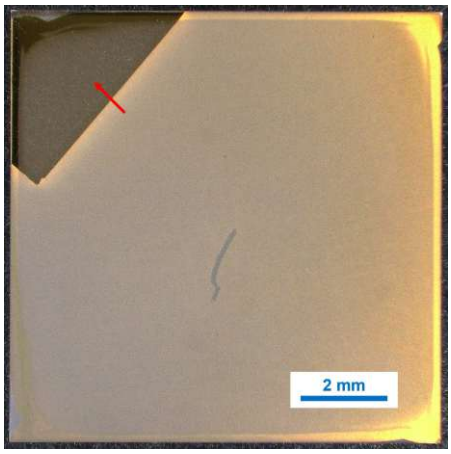

(a) Reference sample with a gold grid and a $LiMn_2O_4$ layer with a free edge.

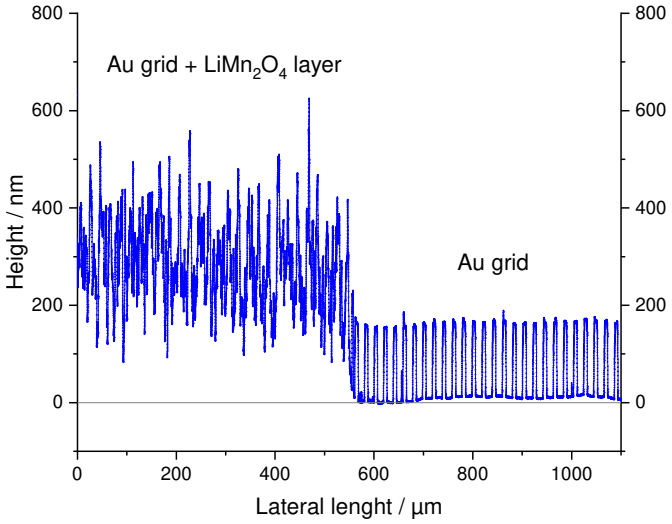

(b) Measured height along a lateral line marked in red in the image on the left.

Figure 29: Results of the profilometer measurement of the reference sample.

The average height of the gold grid was found to be approximately 165 nm. The $LiMn_2O_4$ layer on top results in a total average thickness of 300 nm with a high roughness. This surface morphology can be seen in more details in the scanning electron microscope images (Figure 30).

In Figure 30a the buried gold grid between the YSZ single crystal and the $LiMn_2O_4$ layer can be seen under the thin film. In Figure 30b the pyramid-shaped $LiMn_2O_4$ sputtered crystals can be seen with a higher magnification. In Figure 30c and 30d a cross-section of the thin film is shown, whereby a cross-section of the gold grid is also visible in Figure 30c.

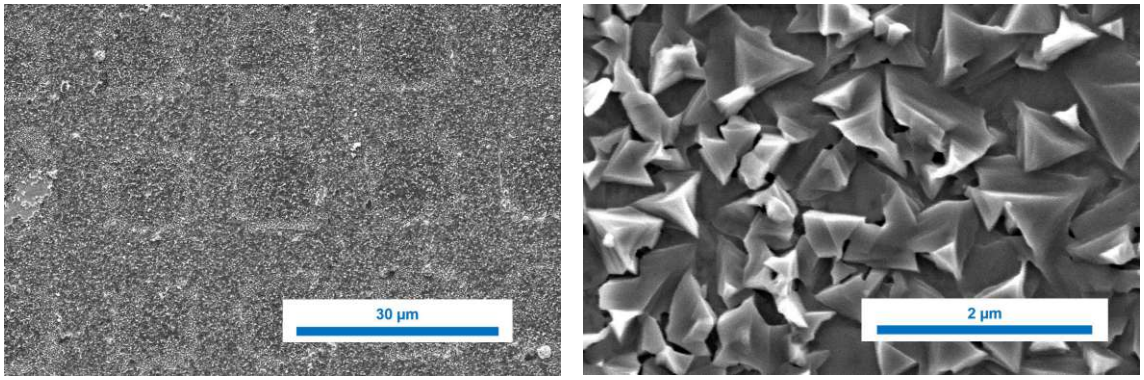

(a) Top-view: Magnification of 5000x.

(b) Top-view: Magnification of 80 000x.

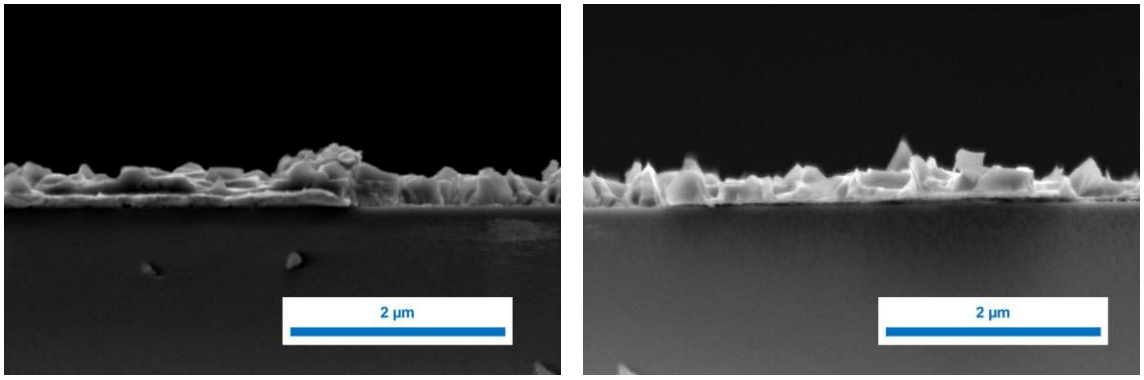

(c) Cross-section: Magnification of 80 000x.

(d) Cross-section: Magnification of 80 000x.

Figure 30: Scanning electron microscope images of the sputtered $LiMn_2O_4$ layer.

The morphology is in line with literature results [42]. Due to the high roughness, a precise determination of the film thickness was not possible here. Therefore, mass spectrometry was used for further characterisation (see Chapter 4.2.3).

4.2.2 Delithiation

Delithiation was conducted to simulate a charged state of LMO in a lithium-ion battery. The current curve corresponding to the applied voltage ramp can be seen for two different delithiations in Figure 31. The potential of a Ag/AgCl electrode in a saturated solution of KCl against the standard hydrogen electrode (SHE) is +0.197 V [48]. In theory, this charge could be used to determine the amount of lithium extracted from the crystal lattice. Due to potential side reactions in the aqueous electrolyte during delithiation, however, the Li-stoichiometry was determined with mass spectrometry (see Chapter 4.2.3).

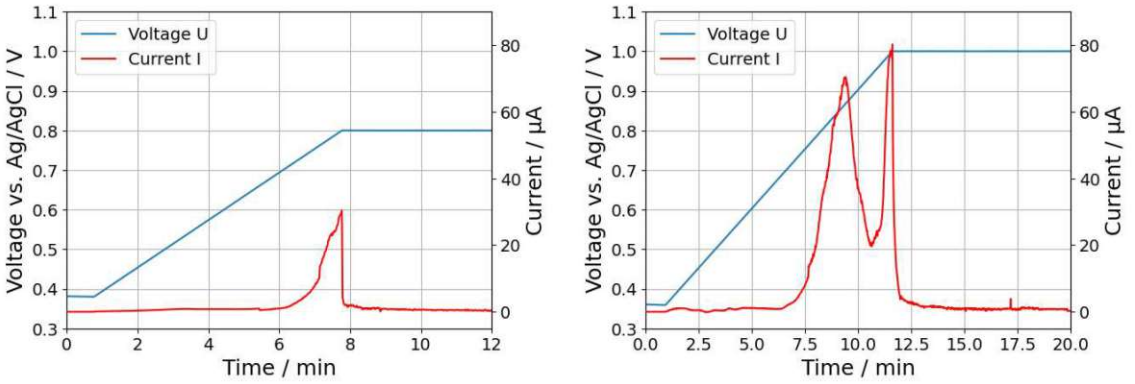

(a) Delithiation to a constant potential of +0.8 V. **(b)** Delithiation to a constant potential of +1.0 V.

Figure 31: Voltage and current curve of the delithiation. The applied voltage was measured against a Ag/AgCl reference electrode.

The current and total charge corresponding to a maximum potential of +0.8 V is much smaller than the current or total charge of the sample with a maximum voltage of +1.0 V. The current starts increasing at a voltage of +0.7 V in both samples. An interesting observation is the shape of the current curve, which indicates two different steps or partial reactions of delithiation which differ by approximately 0.15 V. This is in agreement with the double plateau found for $Li_xMn_2O_4$ [42].

4.2.3 Inductive Coupled Mass Spectrometry

Inductive coupled plasma mass spectrometry (ICP-MS) of the reference samples was performed to assess the sputter rate and Li-stoichiometry after delithiation. The results are listed in Table 4. Li-stoichiometry x in the general formula $Li_xMn_2O_4$ was calculated using Equation 14.

$$x = \frac{2 \cdot n_{\mathrm{Li}}}{n_{\mathrm{Mn}}} \tag{14}$$

x ... Stoichiometric coefficient of Li in the chemical compound $Li_xMn_2O_4$
n_{Li} ... Amount of lithium in mol
n_{Mn} ... Amount of manganese in mol

Table 4: Results of the ICP-MS measurement using three different reference samples with different lithium amount. The first row of each sample belongs to a 1:1000 dilution and the second row to a 1:100 dilution.

No.	Area/mm²	Mass Mn/µg	Mass Li/µg	Thickness/nm	Li-stoichiometry
1	88.0	24.89	1.72	113.5	1.09
		24.15	1.79	110.2	1.17
2	79.1	22.48	1.29	114.0	0.91
		21.36	1.33	108.4	0.98
3	79.0	18.18	0.28	92.4	0.24
		18.67	0.47	94.9	0.40

The area of the sputtered thin film was determined with a light microscope. The masses of manganese and lithium were the results of the ICP-MS measurement. The amount of Mn per sputtered area was calculated to $n_a = 4.79\,\mathrm{nmol\,mm^{-2}}$. With a known density of $LiMn_2O_4$ of $4.1\,\mathrm{g\,cm^{-3}}$ [49] and Equation 15 an effective thickness of the thin film could be calculated. Due to the better signal to noise ratio of the manganese signal, the mass of manganese was used for this calculation.

$$d = \frac{m_{\mathrm{Mn}} \cdot M_{\mathrm{LMO}}}{2 \cdot M_{\mathrm{Mn}} \cdot \rho_{\mathrm{LMO}} \cdot A} \tag{15}$$

d ... Effective thickness of the sputtered thin film in mm
m_{Mn} ... Mass of manganese in mg
M_{LMO} ... Molar mass of $LiMn_2O_4$ in $\mathrm{g\,mol^{-1}}$
M_{Mn} ... Molar mass of manganese in $\mathrm{g\,mol^{-1}}$
ρ_{LMO} ... Density of $LiMn_2O_4$ in $\mathrm{mg\,mm^{-3}}$
A ... Area of the sputtered thin film in $\mathrm{mm^2}$

The average effective thickness of the sputtered $LiMn_2O_4$ thin film was 106 nm. This average thickness was used to normalize the measured charge of the coulometric titrations to a sample volume later on. The results of the Li-stoichiometry combined with the delithiation voltages can be seen in Table 5.

Table 5: Overview of the delithiation process.

Voltage vs. Ag/AgCl	Voltage vs. SHE	Li-stoichiometry
+0.8 V	+1.0 V	$Li_{0.95}Mn_2O_4$
+1.0 V	+1.2 V	$Li_{0.32}Mn_2O_4$

4.2.4 Solid State Coulometric Titration

Coulometric titration was performed for thin film samples of the following stoichiometries according to ICP-MS of reference samples:

- $LiMn_2O_4$
- $Li_{0.95}Mn_2O_4$
- $Li_{0.32}Mn_2O_4$

For each thin film sample, three titration cycles were measured. An example of raw data can be seen in Figure 18 in Chapter 3.2.4, where the data evaluation is documented. In Figure 32 the results of the stoichiometric sample are shown. Analogous to the powder sample, multiple regions with a change in charge at an almost constant voltage are observable. The first one is located around a potential of $-0.8\,V$ (10^{-21} - 10^{-22} bar). The second one is starting at a potential of around $-1.0\,V$. All three cycles (especially the re-oxidation) look very similar. However, for the first reduction an additional minor change in charge at a potential around $-0.4\,V$ is observable. During re-oxidation the curves show two positions where the charge is changing at an almost constant voltage. The first one is at a potential of around $-1.0\,V$ (10^{-28} - 10^{-26} bar). The second one is much sharper and located at a potential between $-0.75\,V$ and $-0.6\,V$ (10^{-17} bar). Like the powder sample the thin film titration curves thus also show a hysteresis.

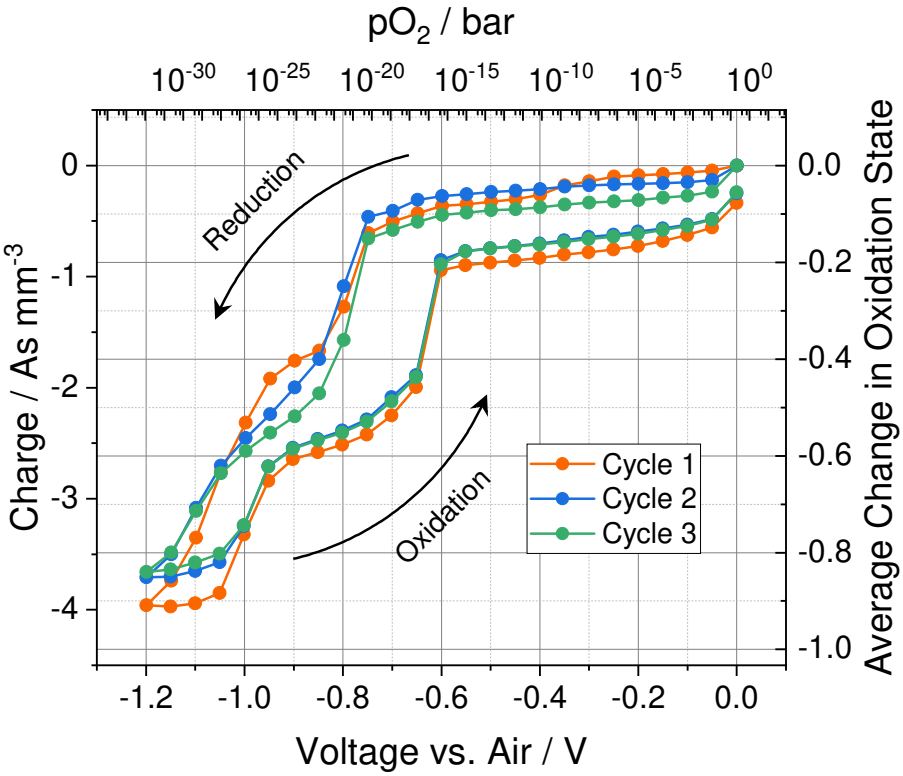

Figure 32: Coulometric titration curve of three cycles of a fully lithiated sample ($LiMn_2O_4$).

These charge changes at almost constant voltages are again interpreted as phase transitions, as already discussed for the titration curve of the powder in Chapter 4.1.2. The second phase transition is probably not finished within this voltage range. The good overlay of all three cycles is in line with the observation from the powder titration that the entire reduction is reversible, as shown with XRD after a whole titration including re-oxidation. Especially in the second part of the titration curve - the re-oxidation - all three curves overlay very well. The additional change in charge during the first reduction might lead to the slightly increased total charge. However, the exact nature of this process could not be determined. The hysteresis could be caused by a different reduction and oxidation kinetic but may also include some differences in the exact reaction path.

In the voltage range between 0 V and −0.75 V the $LiMn_2O_4$ thin film does not undergo any phase transitions during reduction. However, a substantial gradual change in charge was measured in this region indicating formation of significant oxygen non-stoichiometry of the thin film. More specific, a continuos change of the Mn oxidation state of > 0.1 is found, corresponding to a change of δ in $LiMn_2O_{4-\delta}$ by more than 0.1.

These results raise the question which phase transition of the powder samples are also seen in the thin film samples. The comparison between $LiMn_2O_4$ powder and stoichiometric $LiMn_2O_4$ thin film is given in Figure 33.

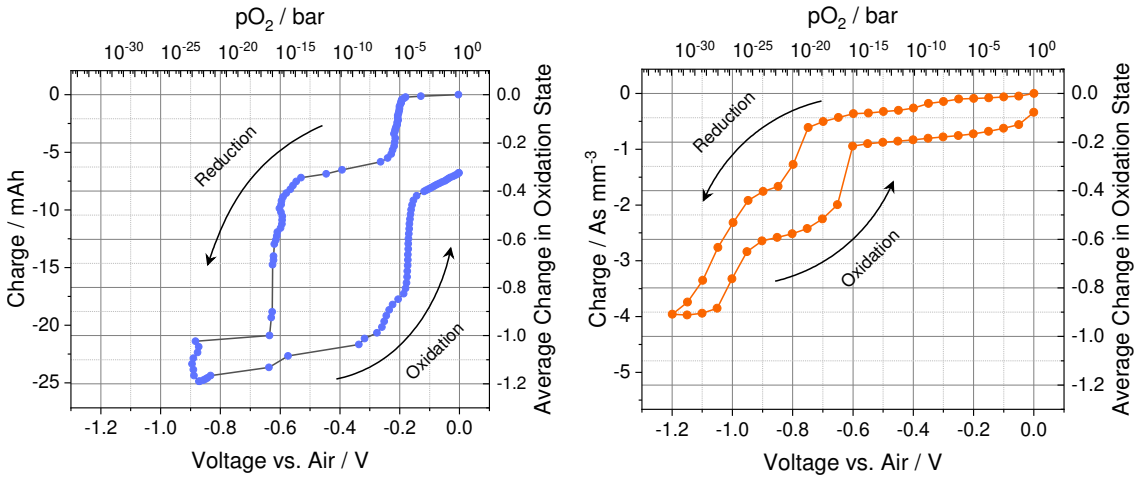

(a) Gas phase coulometric titration of the powder sample.

(b) Solid state coulometric titration of a fully lithiated thin film sample (first cycle).

Figure 33: Comparison of the coulometric titration curve of $LiMn_2O_4$ powder and thin film.

After the first phase transition of both sample types, the plateau in the titration curve is located at an average change in oxidation state of manganese of -0.3 to -0.4 in both graphs. Therefore, these positions are preliminarily assigned to the same state, which means that part of $LiMn_2O_4$ has already decomposed into Mn_3O_4. The immediately following second phase transition covers oxidation state changes from -0.4 to -0.9 and may thus reflect the formation of $LiMnO_2$/MnO. The final decomposition of $LiMnO_2$ does take place in the thin film titration. Phase transitions in the thin film are much less steep than for the gas phase titration.

The biggest difference between the two titration curves is the different potentials of the phase transitions: $-0.8\,V$ vs. $-0.2\,V$ and $-1.0\,V$ vs. $-0.6\,V$ for the second one, both during reduction. This means that in case of the thin film, a much higher over-potential is needed for the same phase transitions. This might be caused by kinetic reasons of the different oxygen removal and uptake mechanisms. In case of the powder, the sample equilibrates with the surrounding gas phase which seems to be faster than the new phase formation and the oxygen remove from the thin film directly through the YSZ electrolyte.

Interestingly, both phase transitions are also found for the re-oxidation, in contrast to the powder sample. This might be due to the fact that $LiMnO_2$ was at least partially decomposed for the powder sample and a reaction of Li_2O and MnO to

form $LiMnO_2$ seems to be kinetically suppressed. Only formation of $LiMn_2O_4$ seems possible. For the thin film sample, $LiMnO_2$ still seems to be present when starting re-oxidation and can be transformed to the spinel. This model, however, does not explain why during re-oxidation of the thin film the phase transitions seem to take place at more negative voltages than during reduction of the powder sample. Possibly non-ideal Li-stoichiometry in the initial $LiMn_2O_4$ thin films could play a role here. This might also cause shifts on the charge axis and thus even the assignment of the phase transitions might change.

Three titration cycles of the delithiated samples are each shown in Figure 34. The charge-axis of the titration plots is scaled the same way as in Figure 32 for a direct comparison of the three different samples. The average change in the oxidation state of manganese was calculated using Equation 16. In contrast to the powder sample where the mass of $LiMn_2O_4$ was known, for the thin film samples the amount of Mn was taken from the ICP-MS measurement.

$$\Delta ON_{\text{av}} = \frac{Q \cdot d}{F \cdot n_a} \tag{16}$$

ΔON_{av} ... Average change of the oxidation number of manganese
Q ... Charge in $\text{C}\,\text{mm}^{-3}$
d ... Average effective thickness in mm
F ... Faraday constant in $\text{C}\,\text{mol}^{-1}$
n_a ... Amount of manganese per sputtered area in $\text{mol}\,\text{mm}^{-2}$

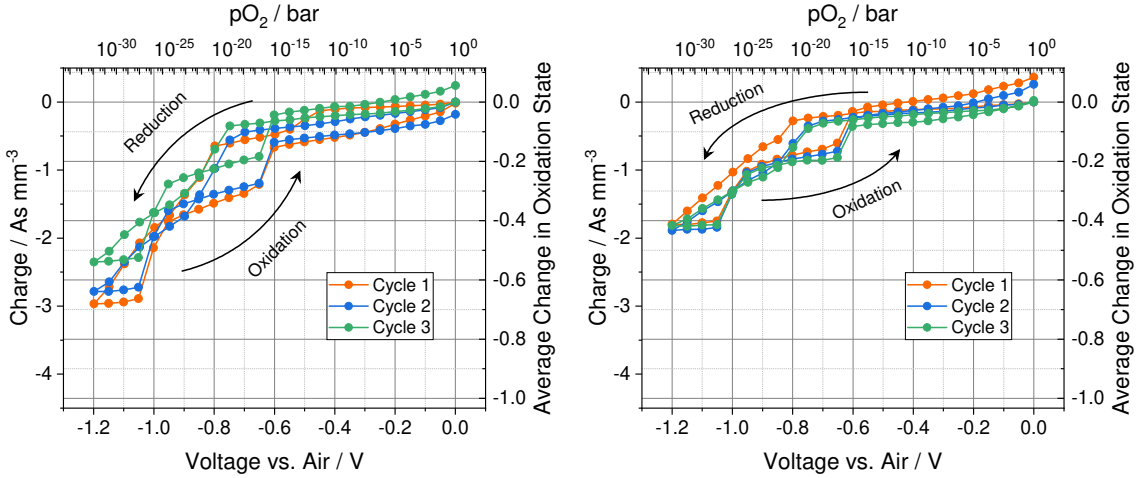

(a) Coulometric titration curve of three cycles of a slightly delithiated sample ($Li_{0.95}Mn_2O_4$).

(b) Coulometric titration curve of three cycles of a delithiated sample ($Li_{0.32}Mn_2O_4$).

Figure 34: Comparison of the titration curves of delithiated thin films with a different Li-stoichiometry.

All three samples exhibit phase transitions at the same potentials, independent of the degree of lithiation. However, the lower the lithium amount of the sample, the less charge can be extracted within each phase transition. The reason for the lower charge is not fully understood yet. However, a potential explanation could be thermal instabilities of delithiated $LiMn_2O_4$. This is known from literature [33] as discussed in Chapter 2.4. The delithiated samples therefore might decompose already during the sealing procedure, i.e. already before the start of the coulometric titration.

4.2.5 Thermal Stability

The dependency of thermal stability of the $LiMn_2O_4$ thin films on the degree of delithiation was studied via XRD. Measurements were performed on reference samples before and after an annealing step at 800 °C for 6 h. That was meant to simulate the sealing procedure. In Figure 35 the 100 % reflection of $LiMn_2O_4$ is shown as a comparison of the three samples before and after annealing.

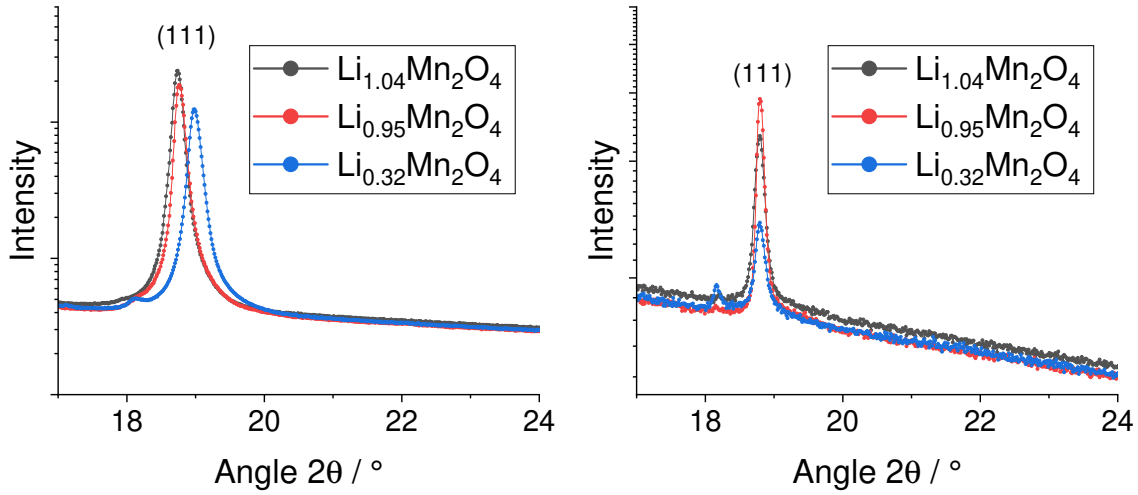

(a) Before annealing. **(b)** After annealing.

Figure 35: Comparison of the 100 % reflection of $Li_{1-\delta}Mn_2O_4$ before and after annealing.

Before annealing a reflection shift dependent on the degree of delithiation was observed. After annealing no more reflection shift was observed. Also the integral of the reflection of the sample with the lowest lithium amount is much lower than the other samples.

A lower amount of lithium in the sample means a higher oxidation number of manganese. This corresponds to a contracted crystal lattice and a higher angle position according to Bragg' law (Equation 17) [50]. An explanation is the higher electric interaction between the more positive manganese and the negative oxygen.

$$n \cdot \lambda = 2 \cdot d \cdot \sin\theta \tag{17}$$

n ... Order of diffraction
λ ... Wavelength of the incident radiation in Å
d ... Interplanar spacing in Å
θ ... Bragg angle in °

A hypothesis is that $Li_xMn_2O_4$ with a low lithium amount is not stable at high temperatures and decomposes into additional phases [33]. In the whole diffractogram of the delithiated sample there were some indications of additional phases, but their intensity were too low for a phase analysis. Therefore it could also be a case of contamination, but these reflections were not measured before the annealing process. Moreover, the interpretation of a diffractogram of a thin film is more complex than that of a powder because of low quantities and preference-orientated growth.

In summary, a potential problem of the measurement setup might be the instability of the delithiated thin film samples at high temperatures. In order to circumvent this issue, the open circuit voltage (OCV) between the thin film and the counter electrode was measured during heating. After delithiation the oxygen amount in the crystal lattice is not in equilibrium with the gas phase, because the chemical potential of lithium has been changed. It was assumed that the counter electrode has the ability to equilibrate with its surrounding atmosphere at lower temperatures than the $LiMn_2O_4$ thin film.

To get electrochemical information about the equilibration process of the $LiMn_2O_4$ electrode, a full lithiated sample was mounted before sealing. Then a temperature ramp of $1\,°C\,min^{-1}$ was applied until 500 °C had been reached and with the same ramp the sample was cooled down. The measured OCV is plotted in Figure 36.

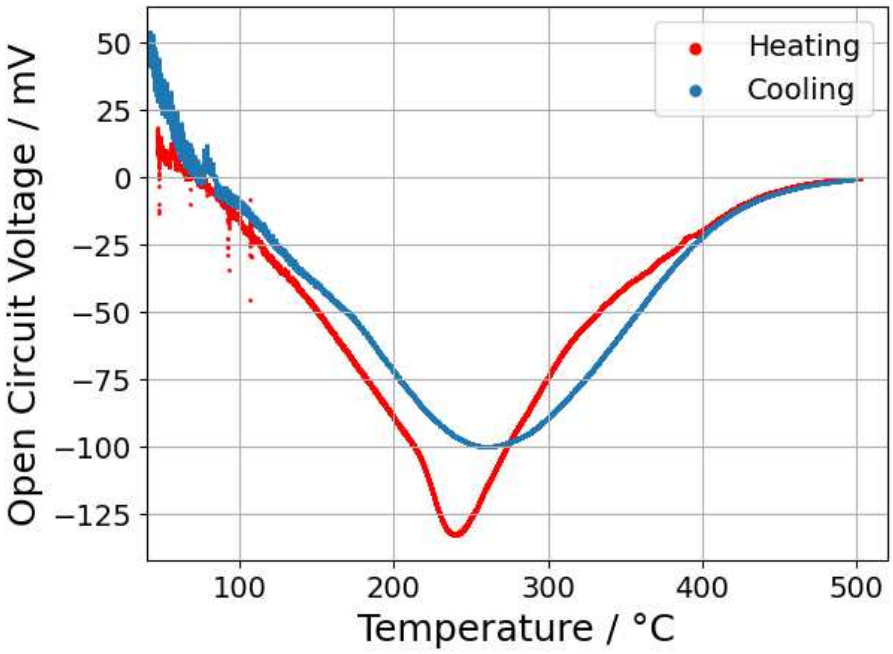

Figure 36: Open circuit voltage during heating and cooling with a temperature ramp of $1\,°C\,min^{-1}$.

The voltage at a temperature below 150 °C is most likely a floating value because the solid state electrolyte (YSZ) is not sufficiently oxygen conductive at low temperatures. At 240 °C the OCV reached a minimum. At 500 °C the voltage between the electrodes is zero.

In contrast to lithium, the oxygen amount in the lattice cannot change at room temperature. The first time after delithiation the sample was heated up, it equilibrated with the atmosphere. This happened during sealing the sample with the glass paste. The measured minimum of OCV at approximately 250 °C suggests that the counter electrode is already in equilibrium with the atmosphere, but the $LiMn_2O_4$ thin film is not. A negative sign of the voltage means that the thin film is more reduced than it would be in equilibrium. The magnitude of the voltage decreases as the temperature rises. This is because the thin film started to equilibrate with the atmosphere. At 500 °C both electrodes are in equilibrium with the atmosphere resulting in a voltage of zero.

5 Conclusion

In this work coulometric titration is shown to be a versatile tool to study oxygen non-stoichiometry and phase stability. It was possible to analyse the oxygen non-stoichiometry and phase stability of the lithium-ion battery cathode material $LiMn_2O_4$ as a powder and as thin films. The powder sample showed three phase transitions at potentials of $-0.2\,V$ (10^{-6} - $10^{-7}\,bar$), $-0.6\,V$ ($10^{-17}\,bar$) and $-0.9\,V$ ($10^{-24}\,bar$). XRD measurements of the powder at specific points on the titration curve revealed the following phase compositions: After the first phase transition, $22\,mol\,\%$ Mn_3O_4 occurred beside Li-enriched $LiMn_2O_4$. The second phase transition led to the formation of $LiMnO_2$ and MnO in the ratio of around $1:1$. The third phase transition was not completed within the covered voltage range. However, at a potential of $-1.25\,V$ ($10^{-35}\,bar$) the powder is shown to be reduced to pure MnO. The re-oxidation to $LiMn_2O_4$ was found to be reversible, though not all phase transitions were present.

$Li_xMn_2O_4$ thin films with varying degrees of delithiation were prepared by sputtering and subsequent delithiation in an aqueous solution. Resulting stoichiometries were assessed with ICP-MS. Phase transitions during coulometric titration were found to be shifted to lower potentials for thin film samples compared to the powder sample. Phase transitions occurred at around $-0.8\,V$ (10^{-21} - $10^{-22}\,bar$) and another one starting at around $-1\,V$ (10^{-26} - $10^{-27}\,bar$). The reason behind this shift in potentials might be different kinetics of the oxygen removal and uptake, which happens through the gas phase in case of the powder and directly through the YSZ single crystal in case of the thin film. For the thin film samples, the positions of phase transitions was found to be independent of the degree of delithiation. However, a decrease of the total charge that could be extracted per phase transition was observed with decreasing lithium content. This is most probably an artefact of sample preparation and caused by the instability of the delithiated samples at elevated temperatures.

6 Outlook

To continue the research of the interplay between the chemical potential of oxygen with the chemical potential of lithium more experiments need to be done. One of the biggest challenges might be the temperature gap between the operating conditions of a lithium-ion battery and a solid state oxygen cell.

One possibility to tackle this issue would be conducting experiments at lower temperatures or to perform measurements as a function of temperature similar to the OCV measurement during heat up in Chapter 4.2.5. To separate kinetic from thermodynamic effects, another approach would be the implementation of discrete temperature steps and change the atmosphere at a fixed temperature where only the counter electrode is equilibrated.

Another approach could be to switch the order of changing the lithium and oxygen amount. In the performed experiments the sample was delithiated before the coulometric titration. One idea would be to change the oxygen amount in the sample at elevated temperatures first, and perform a battery cycle of charge and discharge at room temperature afterwards. These experiments could reveal differences in the performance of $LiMn_2O_4$ used as the cathode of a lithium-ion battery at different oxygen concentrations.

Additionally, another improvement of the experiments would be an extended thin film sample setup. Maybe it is possible to fabricate a double-sided electrochemical cell in the future. One side of the $LiMn_2O_4$ thin film allows oxygen pumping via YSZ and would look like the samples used in this work. The other side of the $LiMn_2O_4$ thin film would look like a lithium-ion battery allowing Li shuttling through a solid state lithium electrolyte.

List of Figures

List of Tables

References

[1] Malgorzata K Gulbinska. *Lithium-ion battery materials and engineering : current topics and problems from the manufacturing perspective*. Green energy and technology. Springer, 2014. DOI: https://doi.org/10.1007/978-1-4471-6548-4.

[2] International Energy Agency. *Batteries and Secure Energy Transitions*. 2024. URL: https://www.iea.org/reports/batteries-and-secure-energy-transitions/outlook-for-battery-demand-and-supply (visited on 07/17/2025).

[3] Yuqing Chen, Yuqiong Kang, Yun Zhao, Li Wang, Jilei Liu, Yanxi Li, Zheng Liang, Xiangming He, Xing Li, Naser Tavajohi, and Baohua Li. "A review of lithium-ion battery safety concerns: The issues, strategies, and testing standards". In: *Journal of Energy Chemistry* 59 (2021), pp. 83–99. DOI: https://doi.org/10.1016/j.jechem.2020.10.017.

[4] McKinsey & Company. *Lithium-ion battery cell demand worldwide in 2022, with a forecast to 2030 (in gigawatt-hours) [Graph]*. In Statista. Jan. 2023. URL: https://www.statista.com/statistics/1419502/global-lithium-ion-battery-demand-forecast/ (visited on 07/17/2025).

[5] Bloomberg. *Projected lithium-ion battery demand worldwide from 2024 to 2028, by application (in terawatt-hours) [Graph]*. In Statista. Aug. 2024. URL: https://www.statista.com/statistics/1488191/projected-demand-of-lithium-ion-batteries/ (visited on 07/17/2025).

[6] QBE Europe. *Fires caused by lithium-ion batteries double in two years*. 2025. URL: https://qbeeurope.com/news-and-events/press-releases/fires-caused-by-lithium-ion-batteries-double-in-two-years/ (visited on 07/18/2025).

[7] Riccardo Amirante, Egidio Cassone, Elia Distaso, and Paolo Tamburrano. "Overview on recent developments in energy storage: Mechanical, electrochemical and hydrogen technologies". In: *Energy Conversion and Management* 132 (2017), pp. 372–387. DOI: https://doi.org/10.1016/j.enconman.2016.11.046.

[8] Nourhan Mohamed and Nageh K. Allam. "Recent Advances in the Design of Cathode Materials for Li-Ion Batteries". In: *RSC Advances* 10.37 (2020), pp. 21662–21685. DOI: https://doi.org/10.1039/D0RA03314F.

[9] Mohammadmahdi Ghiji, Vasily Novozhilov, Khalid Moinuddin, Paul Joseph, Ian Burch, Brigitta Suendermann, and Grant Gamble. "A Review of Lithium-Ion Battery Fire Suppression". In: *Energies* 13.19 (2020), p. 5117. DOI: https://doi.org/10.3390/en13195117.

[10] John B. Goodenough and Kyu-Sung Park. "The Li-Ion Rechargeable Battery: A Perspective". In: *Journal of the American Chemical Society* 135.4 (2013), pp. 1167–1176. DOI: https://doi.org/10.1021/ja3091438.

[11] Ok Kyung Park, Yonghyun Cho, Sanghan Lee, Ho-Chun Yoo, Hyun-Kon Song, and Jaephil Cho. "Who will drive electric vehicles, olivine or spinel?" In: *Energy & Environmental Science* 5.5 (2011), pp. 5111–5120. DOI: https://doi.org/10.1039/C0EE00559B.

[12] Nicholas Pieczonka, Zhongyi Liu, Peng Lu, Keith Olson, John Moote, Bob Powell, and Jung-Hyun Kim. "Understanding Transition-Metal Dissolution Behavior in $LiNi_{0.5}Mn_{1.5}O_4$ High-Voltage Spinel for Lithium Ion Batteries". In: *The Journal of Physical Chemistry C* 117 (Aug. 2013), pp. 15947–15957. DOI: https://doi.org/10.1021/jp405158m.

[13] Yosef Talyosef, Boris Markovsky, Gregory Salitra, Doron Aurbach, Hyeong-jin Kim, and Seungdon Choi. "The study of $LiNi_{0.5}Mn_{1.5}O_4$ 5-V cathodes for Li-ion batteries". In: *Journal of Power Sources* 146.1 (2005), pp. 664–669. DOI: https://doi.org/10.1016/j.jpowsour.2005.03.064.

[14] Andreas Klein and Denis Sudarikov. "The physics of defect chemistry and the chemistry of defect physics". In: *Phys. Chem. Chem. Phys.* 27.13 (2025), pp. 6390–6399. DOI: https://doi.org/10.1039/D4CP04363D.

[15] Ulrich Guth. "Kröger-Vinks Notation of Point Defects". In: *Encyclopedia of Applied Electrochemistry*. Ed. by Gerhard Kreysa, Ken-ichiro Ota, and Robert F. Savinell. New York, NY: Springer New York, 2014, pp. 1159–1160. DOI: https://doi.org/10.1007/978-1-4419-6996-5_310.

[16] Yihua Chen and Huanping Zhou. "Defects chemistry in high-efficiency and stable perovskite solar cells". In: *Journal of Applied Physics* 128.6 (2020), p. 060903. DOI: https://doi.org/10.1063/5.0012384.

[17] Zhendong Guo, Man Yuan, Gaoyuan Chen, Feng Liu, Ruifeng Lu, and Wan-Jian Yin. "Understanding Defects in Perovskite Solar Cells through Computation: Current Knowledge and Future Challenge". In: *Advanced Science* 11.20 (2024), p. 2305799. DOI: https://doi.org/10.1002/advs.202305799.

[18] Alexander Schmid, Ghislain Rupp, and Jürgen Fleig. "Voltage and partial pressure dependent defect chemistry in $(La, Sr)FeO_{3-\delta}$ thin films investigated by chemical capacitance measurements". In: *Physical Chemistry Chemical Physics* 20 (2018). DOI: https://doi.org/10.1039/C7CP07845E.

[19] Qianqian Ji, Lei Bi, Jintao Zhang, Haijie Cao, and X. S. Zhao. "The role of oxygen vacancies of ABO_3 perovskite oxides in the oxygen reduction reaction". In: *Energy Environ. Sci.* 13.5 (2020), pp. 1408–1428. DOI: https://doi.org/10.1039/D0EE00092B.

[20] Yunmin Zhu, Xiao Zhong, Shiguang Jin, Haijun Chen, Zuyun He, Qiuyu Liu, and Yan Chen. "Oxygen defect engineering in double perovskite oxides for effective water oxidation". In: *J. Mater. Chem. A* 8.21 (2020), pp. 10957–10965. DOI: https://doi.org/10.1039/D0TA04362A.

[21] Stephanie E. Wolf, Franziska E. Winterhalder, Vaibhav Vibhu, L. G. J. (Bert) de Haart, Olivier Guillon, Rüdiger-A. Eichel, and Norbert H. Menzler. "Solid oxide electrolysis cells – current material development and industrial application". In: *J. Mater. Chem. A* 11.34 (2023), pp. 17977–18028. DOI: https://doi.org/10.1039/D3TA02161K.

[22] Andrew S. Wills, N. Prasada Raju, and John E. Greedan. "Low-Temperature Structure and Magnetic Properties of the Spinel $LiMn_2O_4$: A Frustrated Antiferromagnet and Cathode Material". In: *Chemistry of Materials* 11.6 (1999), pp. 1510–1518. DOI: https://doi.org/10.1021/cm9810411.

[23] Dennis Becker, Robert Haberkorn, and Guido Kickelbick. "Reactive Milling Induced Structure Changes in Phenylphosphonic Acid Functionalized $LiMn_2O_4$ Nanocrystals – Synthesis, Rietveld Refinement, and Thermal Stability". In: *European Journal of Inorganic Chemistry* 2019.45 (2019), pp. 4835–4845. DOI: https://doi.org/10.1002/ejic.201900946.

[24] Xu Li, Jianchuan Wang, Shiwei Zhang, Lixian Sun, Weibin Zhang, Feng Dang, Hans J. Seifert, and Yong Du. "Intrinsic Defects in $LiMn_2O_4$: First-Principles Calculations". In: *ACS Omega* 6.33 (2021), pp. 21255–21264. DOI: https://doi.org/10.1021/acsomega.1c01162.

[25] Yoshitomo Furushima, Chika Yanagisawa, Takeshi Nakagawa, Yasuhito Aoki, and Naoki Muraki. "Thermal stability and kinetics of delithiated $LiCoO_2$". In: *Journal of Power Sources* 196.4 (2011). DOI: https://doi.org/10.1016/j.jpowsour.2010.09.076.

[26] Jeff R. Dahn, Eric W. Fuller, Marc N. Obrovac, and Ulrich von Sacken. "Thermal stability of Li_xCoO_2, Li_xNiO_2 and λ-MnO_2 and consequences for the safety of Li-ion cells". In: *Solid State Ionics* 69.3 (1994), pp. 265–270. DOI: https://doi.org/10.1016/0167-2738(94)90415-4.

[27] Jan Geder, Harry E. Hoster, Andreas Jossen, Jürgen Garche, and Denis Y.W. Yu. "Impact of active material surface area on thermal stability of $LiCoO_2$ cathode". In: *Journal of Power Sources* 257 (2014), pp. 286–292. DOI: https://doi.org/10.1016/j.jpowsour.2014.01.116.

[28] Tsutomu Ohzuku and Yoshinari Makimura. "Layered Lithium Insertion Material of $LiCo_{1/3}Ni_{1/3}Mn_{1/3}O_2$ for Lithium-Ion Batteries". In: *Chemistry Letters* 30.7 (2001), pp. 642–643. DOI: https://doi.org/10.1246/cl.2001.642.

[29] Ki-Soo Lee, Seung-Taek Myung, Dong-Won Kim, and Yang-Kook Sun. "AlF_3-coated $LiCoO_2$ and $Li[Ni_{1/3}Co_{1/3}Mn_{1/3}]O_2$ blend composite cathode for lithium ion batteries". In: *Journal of Power Sources* 196.16 (2011), pp. 6974–6977. DOI: https://doi.org/10.1016/j.jpowsour.2010.11.014.

[30] Vincenzo Massarotti, Doretta Capsoni, and Marcella Bini. "Stability of $LiMn_2O_4$ and new high temperature phases in air, O_2 and N_2". In: *Solid State Communications* 122.6 (2002), pp. 317–322. DOI: https://doi.org/10.1016/S0038-1098(02)00149-7.

[31] Daichun Tang, Yang Sun, Zhenzhong Yang, Liubin Ben, Lin Gu, and Xuejie Huang. "Surface Structure Evolution of $LiMn_2O_4$ Cathode Material upon Charge/Discharge". In: *Chemistry of Materials* 26.11 (2014), pp. 3535–3543. DOI: https://doi.org/10.1021/cm501125e.

[32] Liubin Ben, Hailong Yu, Bin Chen, Yuyang Chen, Yue Gong, Xinan Yang, Lin Gu, and Xuejie Huang. "Unusual Spinel-to-Layered Transformation in LiMn2O4 Cathode Explained by Electrochemical and Thermal Stability Investigation". In: *ACS Applied Materials & Interfaces* 9.40 (2017), pp. 35463–35475. DOI: https://doi.org/10.1021/acsami.7b11303.

[33] Enyuan Hu, Seong-Min Bak, Jue Liu, Xiqian Yu, Yongning Zhou, Steven N. Ehrlich, Xiao-Qing Yang, and Kyung-Wan Nam. "Oxygen-Release-Related Thermal Stability and Decomposition Pathways of $Li_xNi_{0.5}Mn_{1.5}O_4$ Cathode Materials". In: *Chemistry of Materials* 26.2 (2014), pp. 1108–1118. DOI: https://doi.org/10.1021/cm403400y.

[34] Saiful Islam, Martin R. Busche, Vladimir S. Stubbs, Federico D. Saccone, Rahul Malik, Harry P. C. Tran, Michel B. Decaux, Takeshi Fukutsuka, Tetsu Tatsumi, Ryuichi Kanno, and Mauro Pasta. "Substantial oxygen loss and chemical expansion in lithium-rich layered oxides at moderate delithiation". In: *Nature Materials* 23.6 (2024), pp. 786–793. DOI: https://doi.org/10.1038/s41563-024-02032-6.

[35] Mikhail V. Patrakeev, Ilia A. Leonidov, and Victor L. Kozhevnikov. "Applications of coulometric titration for studies of oxygen non-stoichiometry in oxides". In: *Journal of Solid State Electrochemistry* 15.5 (2011), pp. 931–954. DOI: https://doi.org/10.1007/s10008-010-1111-z.

[36] Martijn H.R. Lankhorst, H.J.M. Bouwmeester, B.A. Boukamp, and H. Verweij. "Oxygen non-stoichiometry and oxygen diffusivity of mixed conducting perovskites". In: *Ceramic Membranes I: Proceedings of the First International Symposium on Ceramic Membranes*. Ed. by H.U. Anderson, A.C. Khandkar, and M. Liu. Vol. 95-24. Proceedings of The Electrochemical Society. Pennington, NJ: Electrochemical Society, 1997, pp. 83–93.

[37] Dieter Barth, Mortaza Sahibzada, and Ian S. Metcalfe. "Novel sensor for studying the transient behaviour of an iron antimonate partial oxidation catalyst". In: *Reaction Kinetics and the Development of Catalytic Processes*. Ed. by G.F. Froment and K.C. Waugh. Vol. 122. Studies in Surface Science and Catalysis. Elsevier, 1999, pp. 403–406. DOI: https://doi.org/10.1016/S0167-2991(99)80172-4.

[38] Elena Markevich, Mikhael D. Levi, and Doran Aurbach. "Comparison between potentiostatic and galvanostatic intermittent titration techniques for determination of chemical diffusion coefficients in ion-insertion electrodes". In: *Journal of Electroanalytical Chemistry* 580.2 (2005), pp. 231–237. DOI: https://doi.org/10.1016/j.jelechem.2005.03.030.

[39] Jong-Hee Park and Robert N. Blumenthal. "Electronic Transport in 8 Mole Percent Y_2O_3-ZrO_2". In: *Journal of The Electrochemical Society* 136.10 (1989), p. 2867. DOI: https://dx.doi.org/10.1149/1.2096302.

[40] Stanislaus Breitwieser, Johannes Bock, Frederick Fechner, Jürgen Fleig, and Andreas Nenning. "Return of the solid-state coulometric titration: A new hope to expand the $p(O_2)$ range". In: *Solid State Ionics* 430 (2025), p. 117001. DOI: https://doi.org/10.1016/j.ssi.2025.117001.

[41] Kerafol Corporation. *Glass Sealing Tapes and Paste KeraGlas ST K03*. 2019. URL: https://www.kerafol.com/wp-content/uploads/2024/07/Kerafol_SOFC_Datenblaetter_Glaslostfolie_Glaspaste_final_05-21.pdf (visited on 06/30/2025).

[42] Andreas E. Bumberger, Christin Boehme, Joseph Ring, Sergej Raznjevic, Zaoli Zhang, Markus Kubicek, and Juergen Fleig. "Defect Chemistry of Spinel Cathode Materials-A Case Study of Epitaxial $LiMn_2O_4$ Thin Films". In: *Chemistry of Materials* 35.13 (2023), pp. 5135–5149. DOI: https://doi.org/10.1021/acs.chemmater.3c00814.

[43] SCHOTT AG. *Datasheet: Alkalifree Barium-borate-glass (Glass-No: GM31107)*. 2022. URL: https://www.schott.com/epackaging (visited on 07/16/2025).

[44] Numpol Meethong, Hanqing Y. S. Huang, W. Craig Carter, and Yet-Ming Chiang. "Galvanostatic Intermittent Titration Technique for Phase-Transformation Electrodes". In: *The Journal of Physical Chemistry C* 113.33 (2009), pp. 13300–13303. DOI: https://doi.org/10.1021/jp9113333.

[45] Janet M. Paulsen and Jeff R. Dahn. "Phase Diagram of Li-Mn-O Spinel in Air". In: *Chemistry of Materials* 11.11 (1999), pp. 3065–3079. DOI: https://doi.org/10.1021/cm9900960.

[46] Damian M. Cupid, Toni Lehmann, Thomas Bergfeldt, Harald Berndt, and Hans J. Seifert. "Investigation of the lithium-rich boundary of the $Li_{1+x}Mn_{2-x}O_4$ cubic spinel phase in air". In: *Journal of Materials Science* 48.9 (2013), pp. 3395–3403. DOI: https://doi.org/10.1007/s10853-012-7126-3.

[47] K. T. Jacob, Anil Kumar, Galla Rajitha, and Yoshio Waseda. "Thermodynamic Data for Mn_3O_4, Mn_2O_3 and MnO_2". In: *High Temperature Materials and Processes* 30.4 (2011), pp. 459–472. DOI: https://doi.org/10.1515/htmp.2011.069.

[48] McAuley Group. *Converting Reference Electrode Potentials*. 2022. URL: https://mcauleygroup.net/article/1/ (visited on 07/11/2025).

[49] Stanford Advanced Materials. *Lithium-Manganat Powder ($LiMn_2O_4$): Specifications*. n.d. URL: https://www.samaterials.de/lithium/1303-lithium-manganate-limn2o4-lithium-manganese-oxide.html (visited on 07/10/2025).

[50] Dong ZhiLi. *Fundamentals of Crystallography, Powder X-ray Diffraction, and Transmission Electron Microscopy for Materials Scientists*. 1st. CRC Press, 2022, pp. 79–80. DOI: https://doi.org/10.1201/9780429351662.